NANO LETTERS

LETTER

pubs.acs.org/NanoLett

Anisotropic Swelling and Fracture of Silicon Nanowires during Lithiation

Xiao Hua Liu,[†] He Zheng,[‡,∠] Li Zhong,[‡] Shan Huang,[§] Khim Karki,[∥] Li Qiang Zhang,[‡,¶] Yang Liu,[†] Akihiro Kushima,[⊥] Wen Tao Liang,[#] Jiang Wei Wang,[‡] Jeong-Hyun Cho,[▽] Eric Epstein,[∥] Shadi A. Dayeh,[▽] S. Tom Picraux,[▽] Ting Zhu,[*,§] Ju Li,[*,⊥,○] John P. Sullivan,[†] John Cumings,[∥] Chunsheng Wang,[◆] Scott X. Mao,[‡] Zhi Zhen Ye,[¶] Sulin Zhang,[#] and Jian Yu Huang[*,†]

[†]Center for Integrated Nanotechnologies, Sandia National Laboratories, Albuquerque, New Mexico 87185, United States

[‡]Department of Mechanical Engineering and Materials Science, University of Pittsburgh, Pittsburgh, Pennsylvania 15261, United States

[§]Woodruff School of Mechanical Engineering, Georgia Institute of Technology, Atlanta, Georgia 30332, United States

[∥]Department of Materials Science and Engineering, University of Maryland, College Park, Maryland 20742, United States

[⊥]Department of Materials Science and Engineering, University of Pennsylvania, Philadelphia, Pennsylvania 19104, United States

[#]Department of Engineering Science and Mechanics, Pennsylvania State University, University Park, Pennsylvania 16802, United States

[▽]Center for Integrated Nanotechnologies, Los Alamos National Laboratory, Los Alamos, New Mexico 87545, United States

[○]State Key Laboratory for Mechanical Behavior of Materials and Frontier Institute of Science and Technology, Xi'an Jiaotong University, Xi'an, 710049, People's Republic of China

[◆]Department of Chemical and Biomolecular Engineering, University of Maryland, College Park, Maryland 20742, United States

[¶]State Key Laboratory of Silicon Materials, Department of Materials Science and Engineering, Zhejiang University, Hangzhou, 310027, People's Republic of China

[∠]Department of Physics, Center for Electron Microscopy and Key Laboratory of Acoustic and Photonic Materials and Devices, Wuhan University, Wuhan 430072, China

Supporting Information

ABSTRACT: We report direct observation of an unexpected anisotropic swelling of Si nanowires during lithiation against either a solid electrolyte with a lithium counter-electrode or a liquid electrolyte with a $LiCoO_2$ counter-electrode. Such anisotropic expansion is attributed to the interfacial processes of accommodating large volumetric strains at the lithiation reaction front that depend sensitively on the crystallographic orientation. This anisotropic swelling results in lithiated Si nanowires with a remarkable dumbbell-shaped cross section, which develops due to plastic flow and an ensuing necking instability that is induced by the tensile hoop stress buildup in the lithiated shell. The plasticity-driven morphological instabilities often lead to fracture in lithiated nanowires, now captured in video. These results provide important insight into the battery degradation mechanisms.

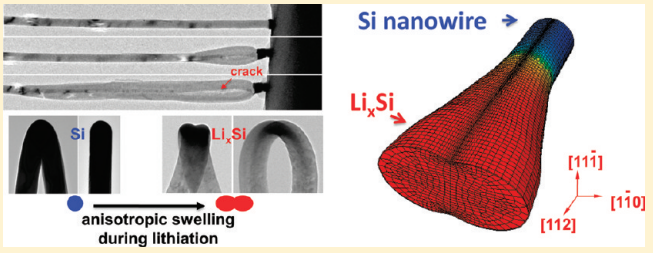

KEYWORDS: Silicon nanowire, lithium ion battery, anisotropic swelling, volume expansion, fracture, in situ TEM

Lithium ion batteries (LIBs) hold great promise for demanding applications such as electric vehicles.[1,2] Silicon is being considered as a candidate anode material in LIBs, as it possesses the highest specific capacity among all materials (~3579 mAh g^{-1} for $Li_{15}Si_4$),[3−6] over an order of magnitude higher than that of carbonaceous anodes used in current LIBs. However, during electrochemical lithiation, Si electrodes experience large volume expansion up to ~300%, leading to pulverization and huge capacity loss even in the first cycle.[1,7−25] While Si has been intensively studied in real and bulk electrochemical cells,[4,5,7−12,15,19,26−32] and impressive colossal volume change was directly observed with in situ optical microscopy and atomic force microscopy,[7,26] it still remains unclear how cracks initiate and evolve at the atomic scale. Although decrease of Si to nanoscale can alleviate pulverization, and nano-Si has been recognized as a promising anode for Li-ion batteries, the poor cyclability still remains and the mechanism behind is not fully understood.[9,10] A fundamental understanding of the deformation and fracture mechanisms in lithiated Si may help develop strategies to accommodate or mitigate the large expansion and crack formation during cycling, thus paving the way for the application of Si as a high energy

Received: May 19, 2011
Revised: June 23, 2011
Published: June 27, 2011

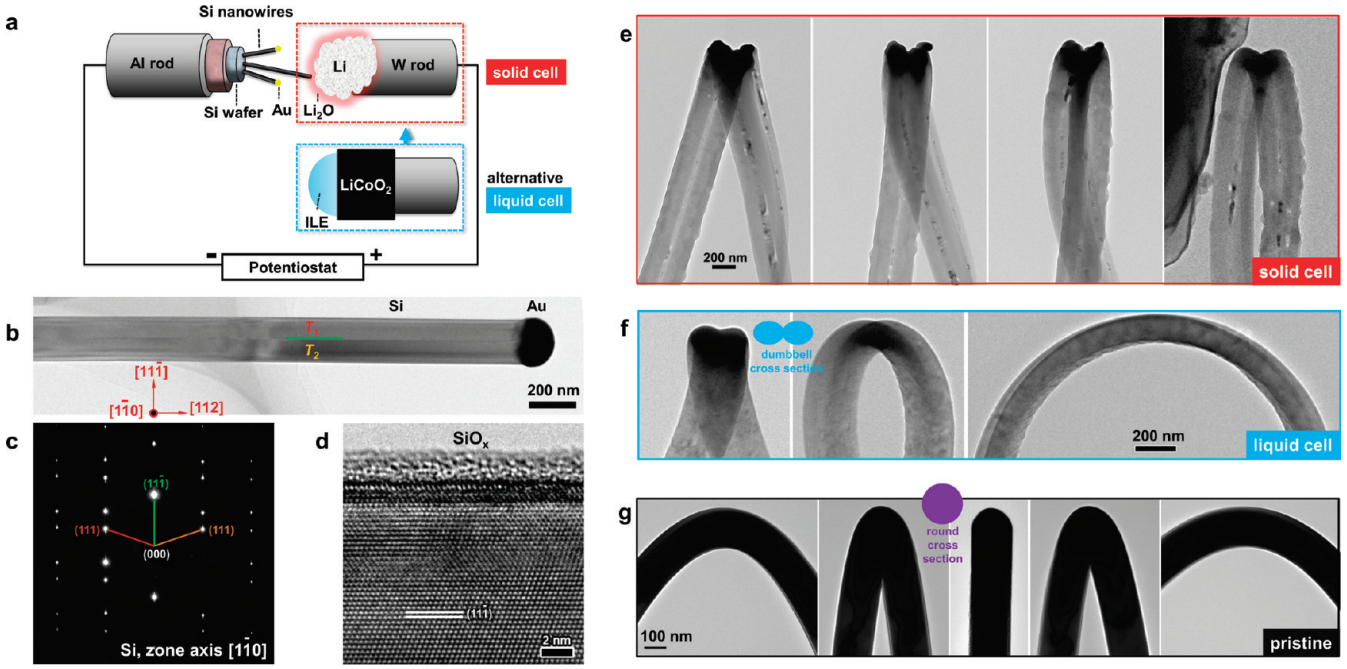

Figure 1. Anisotropic swelling of Si nanowires during lithiation. (a) Schematic illustration of the in situ experimental setup for an all-solid electrochemical cell using Li metal counter electrode ("solid cell") and a "liquid cell" using the ionic liquid electrolyte and $LiCoO_2$ counter-electrode for Si lithiation tests. (b−d) Microstructure of a typical pristine Si nanowire. The nanowire had uniform diameter and a twin boundary in the center (b), consistent with the electron diffraction pattern (EDP) in (c). There was a 2 nm thick native amorphous oxide layer on the surface (d). (e−g) Tilted series images showing the same dumbbell shape of the lithiated Si nanowires in a solid cell (e) or in a liquid cell (f), in contrast to the round cross section of the pristine Si nanowire (g).

density electrode in LIBs.[33−35] In this development, from both practical and fundamental standpoints, what happens to crystalline silicon in the first cycle of lithiation is critically important.

We report here anisotropic swelling of Si nanowires during lithiation in either a conventional liquid cell or an all-solid electrochemical cell inside a transmission electron microscope (TEM), with the latter consisting of a single Si nanowire working-electrode, a nonconventional Li_2O solid electrolyte, and a bulk Li metal counter-electrode. Figure 1a shows the schematic illustration of our experimental setup. Fresh Li metal was loaded as the Li source and reference electrode in the solid cell. Compared to our previous experimental setup (i.e., the liquid cell) where an ionic liquid electrolyte (ILE) was used,[3,33,36−38] the solid cell configuration offers the advantage of one-dimensional Li transport along the Si nanowire and directly observing the microstructure evolution from the very beginning of the lithiation process. A naturally grown Li_2O layer (∼700 nm thick) was formed on the surface of the Li metal by air exposure (∼2 s) and used as solid electrolyte between the Si working and Li counter-electrodes (Figure S1, Supporting Information). Si nanowires that were grown by vapor−liquid−solid growth (VLS) from Au catalyst islands on a Si wafer were affixed to a scanning tunneling microscopic (STM) probe and then translated via piezopositioners to approach the Li_2O electrolyte using Li counter-electrode. Panels b−d of Figures 1 show the typical microstructure of the pristine Si nanowires used in this study. The Si nanowires were grown along the [112] direction, usually with a 180° twin boundary parallel to the (11$\bar{1}$) plane (Figure 1b, c) and a 2 nm thick native oxide layer on the surface (Figure 1d). Because the Li_2O layer formed a large barrier for Li^+ transport,[39] a potential of −2 V applied to the Si nanowire versus the Li counter electrode was necessary to promote lithiation of the Si nanowire, significantly deviated from the 0 to +2 V (versus Li) window used in a conventional Li−Si half-cell. This large negative potential is different from a standard Li battery, due to a potential drop needed for activated ionic transport in the Li_2O, which does not have high Li^+ ion conductivity at room temperature.[40,41] However, as we show below, once the lithium reaches the silicon, the diffusion and reaction do not depend on the lithium source and the battery setup (regardless of the liquid or solid cells), and the behavior is intrinsic to the crystal structure of the host silicon nanowire.

Interestingly, the volumetric expansion of the Si nanowire after lithiation in the solid cell was highly anisotropic, exhibiting a dumbbell-shaped cross section (Figure 1e, movies S1−S3 in the Supporting Information). To test whether the anisotropic volumetric expansion was related to the contact geometry between the nanowire and the solid electrolyte, we performed lithiation tests of the same batch of Si nanowires with a liquid cell in a flooding geometry (with the entire nanowire immersed in the liquid electrolyte). Similar anisotropic volumetric expansion and phase transformation to that in a solid cell was also observed in the liquid cell (Figure 1f), and both are in sharp contrast to the round shape of the pristine Si nanowires (Figure 1g), indicating that the phase transformation and deformation were intrinsic to the process of Li insertion into Si. This result also verifies that the dumbbell shape is independent of the lithium sources (from either Li or $LiCoO_2$), lithium transport media (Li_2O, Li_xAu or an electrolyte containing lithium salts), or lithiation conditions such as applied mechanical loading states, i.e., disregarding the stress of the nanowires pushing against the solid Li counter-electrode or merely immersed stress-free in the liquid electrolyte. Hence,

dx.doi.org/10.1021/nl201684d |*Nano Lett.* 2011, 11, 3312–3318

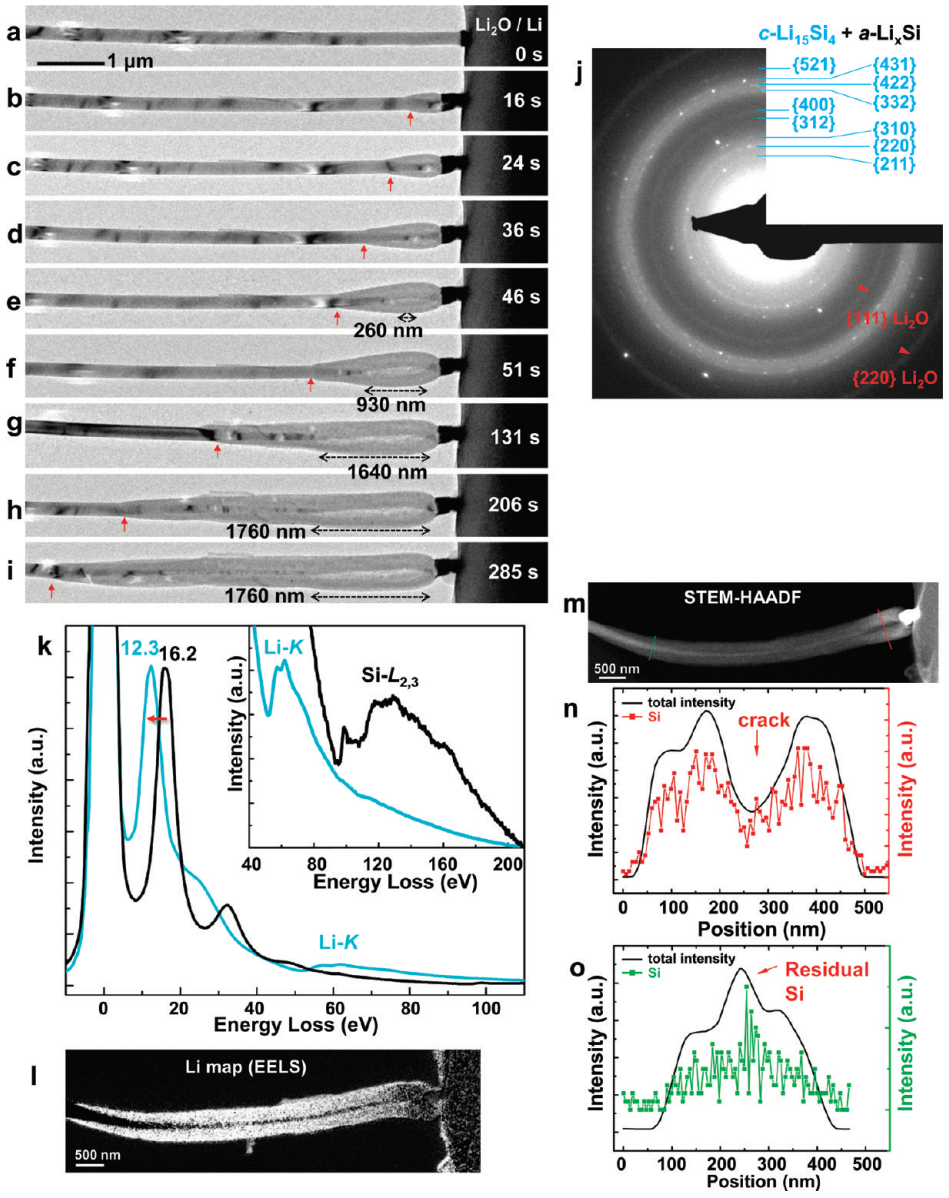

Figure 2. Crack formation of a lithiated silicon nanowire. (a−i) Morphology evolution of the Si nanowire during lithiation in the solid cell. Shortly after contacting the Li_2O/Li electrode, the Au cap was lithiated and elongated (b) followed by lithiation of the Si nanowire (b−i). The red arrows mark the reaction fronts at different stages. The diameter increased from 216 nm of the pristine nanowire to 580 nm of the lithiated wire close to the Au cap. A crack developed as the residual Si core was depleted (e−i). (j) EDP showing the formation of polycrystalline $Li_{15}Si_4$ (*c*-$Li_{15}Si_4$), Li_2O, and an amorphous Li_xSi (*a*-Li_xSi) alloy. (k) Comparison of the electron energy loss spectra (EELS) of the pristine and lithiated Si nanowires. The primary plasmon peak shifted from 16.2 to 12.3 eV (marked by the red arrow). The inset spectra show that the Li K-edge peak emerged at ∼55 eV and Si L-edge decreased significantly in 99−150 eV. (l) Lithium map by EELS showing the predominant lithium distribution in the $Li_{15}Si_4$ shell. The *c*-Si core shows dark contrast, indicating little lithium present. The mapping was obtained using a spectrum imaging technique in Digital Micrograph. The energy filter for Li K-edge was from 40 to 80 eV with a step of 3 eV. The Si L-edge was outside of the energy window, thus the Si signal was negligible. (m) STEM-HAADF image of the nanowire. The crack showed dark contrast, indicating less material (lower average *Z*) present. The STEM image was collected with a camera length of 120 mm. (n, o) Line scans along the red and green lines in (m), respectively, showing the total intensity profile which is proportional to the sample mass thickness (dark lines), and Si K_α EDX intensity profile (red and green lines in (n) and (o), respectively), confirming the presence of a crack (n) and a residual *c*-Si core (o) from the lithiated nanowire.

the results reflect an intrinsic solid-state Li−Si alloying process at ambient temperature.

Figure 2 shows the microstructure evolution and characterization of a Si nanowire upon lithiation in a solid cell. A few seconds after the Si nanowire with a gold catalyst particle on its tip touches the Li_2O (Figure 2a), lithiation initiates at the Au cap, leading to its elongation (Figure 2b). Lithiation then propagates to the Si nanowire (Figure 2b), and a reaction front (pointed out by red arrows in panels b−i of Figure 2) propagates progressively along the axis of the nanowire. During this reaction, lithiation near the outer surface of the nanowire proceeds faster than that near the center, resulting in the formation of a lithiated shell with an

dx.doi.org/10.1021/nl201684d |*Nano Lett.* 2011, 11, 3312–3318

unreacted crystalline Si (*c*-Si) core. Huge deformation of the gold cap was observed in both the solid and liquid cells, but lithiation of Si nanowires does not appear to be altered by the presence of the gold particles in either case (Figure S2, Supporting Information). The unreacted *c*-Si core exhibits a tapering shape, with its diameter decreasing in the direction from the reaction front toward the point of initial contact. For the nanowire shown in Figure 2, at the point the *c*-Si core disappears, i.e., where the Si was completely amorphized by lithium insertion, a nanocrack formed (Figure 2e). The crack continues to grow as the lithiation front progresses further along the wire (Figure 2e−i and Figure S3 and Movies S4−S6 in the Supporting Information). Within about 200 s, the crack length grows from 260 to 1640 nm during the initial lithiation stage (Figure 2e−g), but then crack growth stops as the *c*-Si core is not completely consumed (Figure 2g−i). Through the application of a positive potential (+2 V) on the Si nanowire with respect to the Li counter-electrode, the lithiated Si nanowire can be delithiated and the crack length decreased (Figure S4, Supporting Information).

To characterize the lithiated nanowire, electron diffraction patterns (EDPs) were captured that indicate the coexistence of the crystalline $Li_{15}Si_4$ (*c*-$Li_{15}Si_4$) and Li_2O phases, as well as the amorphous Li_xSi (*a*-Li_xSi) alloy (Figure 2j). Identification of *c*-$Li_{15}Si_4$ as the fully lithiated phase,[3] consistent with previous in situ X-ray diffraction measurements,[4,5,20,27] was made by rigorous diffraction analyses in comparison with simulations of the seven known crystalline Li_xSi phases, including LiSi ($x = 1$), $Li_{12}Si_7$ ($x = 1.71$), Li_7Si_3 ($x = 2.33$), $Li_{13}Si_4$ ($x = 3.25$), $Li_{15}Si_4$ ($x = 3.75$), $Li_{21}Si_5$ ($x = 4.2$), and $Li_{22}Si_5$ ($x = 4.4$);[16,42] see details in the Supporting Information (Figure S5). The EDP *d*-spacing and the diffraction intensity obtained from our experiments match excellently with that of the *c*-$Li_{15}Si_4$ phase. The formation of Li_xSi alloy is also characterized by significant changes in the electron energy loss spectra (EELS) of the Si nanowire after lithiation (Figure 2k): (1) the primary plasmon peak shifts from 16.2 eV down to 12.3 eV (indicated by the red arrow); (2) the Si L-edge significantly decreases (inset of Figure 2k, onset at ∼99 eV); and (3) the Li K-edge emerges around 55 eV as the dominant peak in 40−240 eV range. The energy resolution of our spectrometer is 1.5 eV (dispersion: 0.3 eV/channel). The Li distribution map in the energy loss window (40−80 eV, well below the onset of Si-$L_{2,3}$ edge at 99 eV) shows a clear picture of the lithiated shell and the unreacted *c*-Si core. The results are consistent with scanning transmission electron microscopy high angle annular dark field (STEM-HAADF) imaging (Figure 2m), showing the *Z* contrast (*Z*: atomic number) of the nanowire. In the central dark region near the nanowire tip, the core shows a reduction in high-*Z* Si ($Z = 14$), confirming the formation of a crack in the center of the lithiated section of the nanowire. Panels n and o of Figure 2 show line scans across the crack (red lines in panels m and n of Figure 2) and the partially lithiated part (green lines in Figure 2m,o) of the nanowire, respectively. The crack is revealed by an intensity dip in both the *Z*-contrast intensity (black line in Figure 2n) and the Si Kα (1.7 keV) energy-dispersive X-ray spectroscopy (EDX) intensity (red trace in Figure 2n). In contrast, Figure 2o indicates that average *Z* is significantly lower in the $Li_{15}Si_4$ shell than in the residual *c*-Si core due to the low *Z* of lithium ($Z = 3$) and the much diluted atomic concentration of Si (∼21%) in the alloy shell.

Figure 3 shows the crystallography of the anisotropic expansion in another Si nanowire during lithiation. The pristine Si nanowire had uniform diameter and a twin boundary parallel to

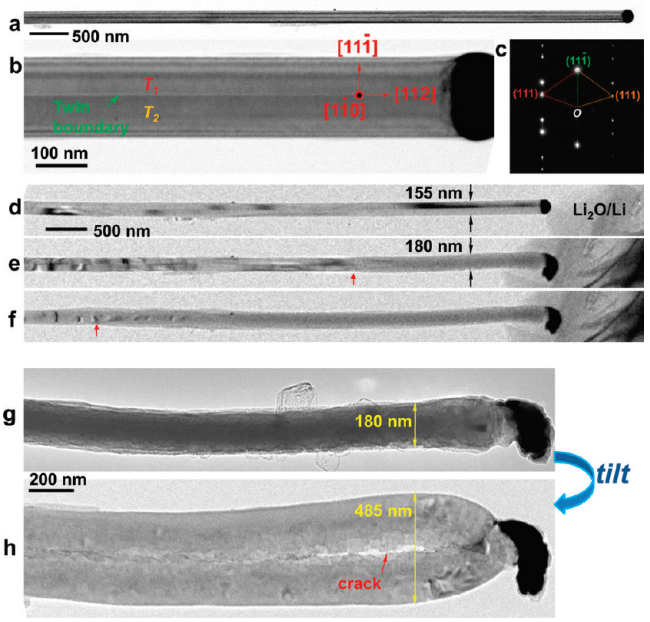

Figure 3. Anisotropic swelling and crack formation of Si nanowire during lithiation. (a) Pristine straight Si nanowire with uniform diameter. (b) High magnification image of the pristine Si nanowire with a visible twin boundary in the center. (c) EDP showing the twin viewed along the [1$\bar{1}$0] zone axis. The axis of the nanowire was along [112], and the twin boundary was parallel to (11$\bar{1}$). (d−f) Lithiation of the Si nanowire. The visible diameter expansion was only 17% and no elongation was observed. The red arrows mark the longitudinal reaction fronts. Note the contrast of the image changed from single crystalline to that of gray polycrystalline. (g, h) Lithiated nanowire in (f) viewed along $[1\bar{1}0]_{Si}$ (g) and close to $[11\bar{1}]_{Si}$ (h) directions, respectively, showing the anisotropic volumetric expansion.

the axis (Figure 3a,b). The EDP confirmed the following same orthogonal directions as that shown in Figure 1b−d: [112] was the growth direction; [11$\bar{1}$] was the norm of the twin boundary; [1$\bar{1}$0] was the electron beam incident direction (Figure 3b,c). Viewed from the [1$\bar{1}$0] direction, lithiation of the nanowire revealed only a 17% diameter expansion, from the original 155 to 180 nm (Figure 3d−f). However, tilting of the lithiated nanowire to a viewing direction closer to [11$\bar{1}$] showed a much larger expansion (from the original 155 to 485 nm, Figure 3g,h) and also an obvious crack in the center of the nanowire (Figure 3h). Observations on other nanowires confirmed the same anisotropic expansion: the diameter expands by ∼170% along ⟨110⟩ but less than 20% along ⟨111⟩ directions (Figure S6, Supporting Information). It is worth noting that the planar defect, i.e., the twin boundary parallel to the (11$\bar{1}$) plane, was not the cause of the anisotropic deformation, as the twin boundary was parallel to the long axis of the dumbbell rather than the short axis. In other words, a single twin (T_1 or T_2) itself also underwent the anisotropic deformation upon lithiation. Hence, we conclude that the twin boundary does not affect the lithiation and swelling, as might be expected since the atomic structure of coherent twin boundary requires no disruption of the covalent sp^3 bonding of silicon.

We conducted lithiation on many Si nanowires, with all showing consistent anisotropic volumetric expansion. The reaction front migration distance *L* was measured for both solid-cell and liquid-cell lithiation, which was found to be approximately linear with respect to the reaction time, $L \propto t$ (Figure 4). This

dx.doi.org/10.1021/nl201684d |*Nano Lett.* 2011, 11, 3312–3318

indicates that the kinetics of lithiation are likely controlled by short-ranged processes near the reaction front (interfacial diffusion and reaction, with adjacent plastic flow), and not by long-ranged diffusive transport along the length of the wire. This is in sharp contrast to the $L \propto t^{1/2}$ behavior found in the lithiation of SnO_2 nanowires in prior studies using a liquid-cell setup.[33] Intriguingly, crack-induced fracture of the $Li_{15}Si_4$ nanowire was also observed at some extreme situations (Figure S7, Supporting Information). Figure S7a shows a split $Li_{15}Si_4$ nanowire in the fast lithiation process polarized at −4 V against Li metal. The nanowire was fractured into two subwires (Figure S7b−d) along the central crack (Figure S7e). Due to the limitations against such strong electric potentials in the liquid cell geometry, a similar self-splitting phenomenon has not been observed in that case, but the fracture phenomenon shows a clear link to the more common anisotropic swelling phenomenon observed in all conditions. In cases when the Li_2O electrical isolation layer is not thick enough, and we see a short circuit between the Si nanowire and the Li metal, then the lithiation proceeds rapidly at 0 V applied potential with the same fracture phenomenon. Thus, we conclude that the fracture is related to the fast lithiation of the nanowire and not the strong potential (−4 V) used in the solid cell.

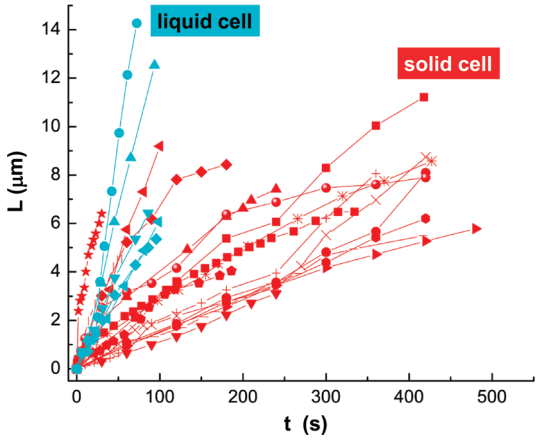

Figure 4. Statistics of the reacted Si nanowire length (L) versus time (t) plot. The linear $L-t$ relationship was observed for both the solid and the liquid cells for the same batch of Si nanowires. The reaction front migration speed was about 10−200 nm/s in the solid cell and about 60−200 nm/s in the liquid cell. The larger variation of the speed in the solid cell was likely due to the variation of Li^+ transport in the Li_2O electrolyte.

To understand the anisotropic swelling and fracture in the lithiated nanowire, we modeled Li diffusion coupled to elasto-plastic deformation (Figure 5a). The diffusion was described by a nonlinear model (Supporting Information) with diffusivities depending on the local Li concentration, giving an evolving core−shell structure with the sharp interface separating a Li-deficient core (ratio of Li to Si, $x \approx 0$) and Li-rich shell ($x \approx 3.75$). Figure 5b shows the simulated Li distribution in the wire, demonstrating the progressive development of the three-dimensional tapered c-Si core (Figure 5c). Numerical studies indicate that the small taper of the core is the manifestation of faster Li diffusion on the cylindrical surface than in the bulk of the wire, as suggested by the recent first principles calculations of lithium migration barriers.[12] To capture the anisotropic dimensional change of the cross section, we have matched the model to the observed cross-sectional shape by using an appropriate anisotropic lithiation-induced strain, i.e., 150% in $[1\bar{1}0]$ and 40% in $[11\bar{1}]$ at the lithiation limit of $x = 3.75$ (see Figure S8c, Supporting Information). Moreover, our model indicates that the lithiation reaction front (i.e., the core−shell interface) should move much faster in the $[1\bar{1}0]$ direction than $[11\bar{1}]$, in order to facilitate the development of dumbbell-shaped cross sections in finite element calculations (Figure S9, Supporting Information). Such anisotropy in migration velocity of the reaction front was realized numerically by assigning the anisotropic Li diffusivities.

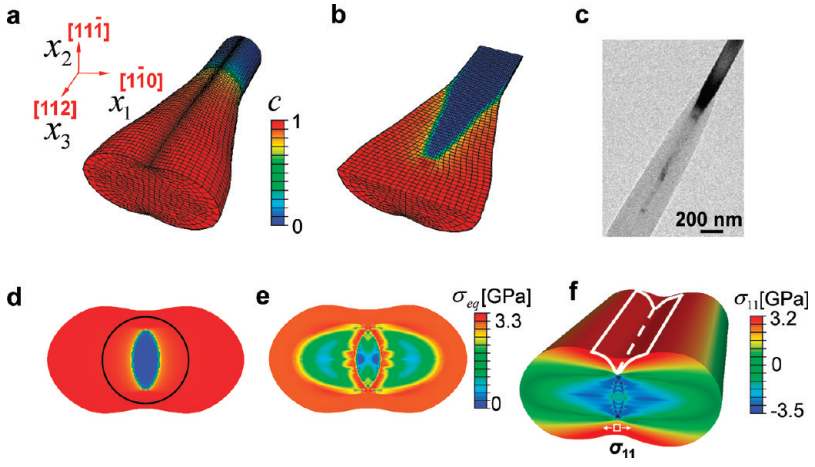

Figure 5. Simulated Li and stress distributions in a [112]-oriented Si nanowire. (a) 3D simulation of a progressively lithiated nanowire (i.e., the Li flux is prescribed at the front end), showing the development of the dumbbell-shaped cross section along the longitudinal direction. The contour indicates the normalized Li concentration, c, defined as the actual Li concentration divided by the Li concentration in the fully lithiated state ($x = 3.75$). (b) The wire is cut to expose the Li distribution in the $(11\bar{1})$ cross section, showing the tapered Si core structure, which is consistent with the TEM image of (c). (d) The Li distribution, c, in the (112) cross section at a representative postnecking stage, showing the $[11\bar{1}]$-elongated Si core. The black circle indicates the initial cross section of the pristine Si nanowire. (e) Distribution of the von Mises equivalent stress, $\sigma_{eq} = (3\sigma_{ij}\sigma_{ij}/2)^{1/2}$, corresponding to the Li distribution in (d); the areas in red attain plastic yielding. (f) Schematic of neck growth along the longitudinal direction of the nanowire. The front cross section shows the distribution of the normal stress component, σ_{11}. At the plane of $x_1 = 0$, σ_{11} is tensile near the surface indent and compressive in the center, the diminishing of central compression with increasing indent facilitates unstable necking growth (indicated by white lines) that can progress to form cracks.

dx.doi.org/10.1021/nl201684d |*Nano Lett.* 2011, 11, 3312–3318

That is, the apparent Li diffusivity in the (112) cross section was taken to be 100 times larger in $[1\bar{1}0]$ than in $[11\bar{1}]$. It should be emphasized that the assignment of anisotropic diffusivities in our diffusion simulation serves as an effective numerical approach to capture the crystal orientation-dependent migration velocity of the reaction front, which is actually a two-phase boundary separating the *crystalline* core and *amorphous* shell (see Supporting Information). The physical origin of large anisotropies of the lithiation strain and migration velocity of the reaction front is not well understood yet. However, it is expected to be controlled by the atomic processes of accommodating large volumetric strains at the crystal−amorphous interface that depend sensitively on the crystallographic orientation; similar interface-mediated anisotropic responses have been observed in both oxidation and wet etching of *c*-Si.[43−45] Understanding their mechanistic basis requires a systematic study of lithiation reactions,[46] accounting for factors such as the interfacial energy and reactive layer,[47] the bond density and states near the interface,[43] stress effects on reaction and diffusivity,[48,49] etc.

The progressive lithiation causes the buildup of high stresses, leading to plastic flow and fracture in the wire. In a first approximation, we adopted an elastic perfectly plastic model with a yield stress of 3 GPa.[50] Our simulations (Movies S7−S10, Supporting Information) clearly show the lithiation-induced anisotropic expansion, plastic flow of the lithiated shell, and onset of necking instability, leading to the formation of a dumbbell-shaped cross section. The table in Figure S8c lists the simulated cross-sectional geometry of a fully lithiated wire, consistent with experimental measurements. Figure 5d shows the core−shell structure with a sharp lithiation reaction front at a postnecking stage, and Figure 5e shows the corresponding contour of the von Mises stress (red indicates attainment of the plastic yield stress). In the experiments (Figure 2), the formation of surface cracks was observed at the cross section, in the region where the *c*-Si core was fully amorphized. To explain this fracture mode, we note that the present necking instability is driven by the internal expansion associated with lithiation of the Si core. Because of the absence of the external load, the resultant stress integral on any plane of the wire has to be zero, such that both the tensile and compressive stresses must coexist. Figure 5f confirms this by showing the distribution of the stress component normal to the nanowire axis, σ_{11}, at a typical postnecking deformation stage; on a central x_2-x_3 plane ($x_1 = 0$). The stress is tensile near the surface indent and compressive in the Si core (Figure S10c,d, Supporting Information). The former tends to drive the growth of the neck and facilitate the initiation of a surface crack, while the latter resists this crack initiation. As lithiation proceeds, the *c*-Si core is reduced, leading to diminishment of the region of compressive stress. The vanishing compressive stresses near the center of the wire allow the unstable growth of the indent that progresses to form cracks and may eventually lead to a splitting of the wire (Figure S7, Supporting Information).

Our detailed observations and modeling have several important implications for the development of Si anode materials for LIBs. First, lithiation of crystalline Si leads to highly anisotropic transformation strains of the $Li_{15}Si_4$ product which promote fracture, but this process could be mitigated. For example, orienting the nanowires along a ⟨110⟩ crystallographic axis could promote wire lengthening as the primary volumetric expansion mechanism. Second, if conductive coatings are applied to the surface of the nanowires, these coatings are more likely to remain intact along ⟨111⟩-containing surfaces of the nanowire, as the expansion is lower in the ⟨111⟩ directions. Third, the use of amorphous Si as an anode material would likely remove the anisotropy associated with initial lithiation and could suppress fracture.

CONCLUSIONS

Taking advantage of the electron transparency of nanowires, we performed real-time in situ TEM observations of the lithiation of Si nanowires to identify the morphology changes associated with lithiation. We have directly observed that the large volumetric expansion as Si converts to $Li_{15}Si_4$ occurs in a highly anisotropic fashion in free-standing nanowires of ⟨112⟩ growth directions, resulting in intermediate dumbbell-shaped cross sections. Despite extensive plastic flow of the lithiation product, very large tensile stresses nevertheless develop inside the nanowire during Li insertion, causing a necking instability and fracture.

ASSOCIATED CONTENT

Supporting Information. Experimental details for Si nanowire preparation, in situ electrochemical devices construction, electron microscopy, and modeling. This material is available free of charge via the Internet at http://pubs.acs.org.

AUTHOR INFORMATION

Corresponding Author

*E-mail: jhuang@sandia.gov, ting.zhu@me.gatech.edu, liju@seas.upenn.edu.

ACKNOWLEDGMENT

Portions of this work were supported by a Laboratory Directed Research and Development (LDRD) project at Sandia National Laboratories (SNL) and partly by Nanostructures for Electrical Energy Storage (NEES), an Energy Frontier Research Center (EFRC) funded by the U.S. Department of Energy, Office of Science, Office of Basic Energy Sciences under Award Number DESC0001160. The LDRD supported the development and fabrication of platforms. The NEES center supported the development of TEM techniques. CINT supported the TEM capability; in addition, this work represents the efforts of several CINT users, primarily those with affiliation external to Sandia National Laboratories. In addition, this work was performed, in part, at the Sandia−Los Alamos Center for Integrated Nanotechnologies (CINT), a U.S. Department of Energy, Office of Basic Energy Sciences user facility. Sandia National Laboratories is a multiprogram laboratory operated by Sandia Corporation, a wholly owned subsidiary of Lockheed Martin Company, for the U.S. Department of Energy's National Nuclear Security Administration under Contract DE-AC04-94AL85000. T.Z. acknowledges the support by NSF Grants CMMI-0758554 and CMMI-0825435. A.K. and J.L. acknowledge support by NSF DMR-1008104 and AFOSR FA9550-08-1-0325.

REFERENCES

(1) Arico, A. S.; Bruce, P.; Scrosati, B.; Tarascon, J. M.; Van Schalkwijk, W. *Nat. Mater.* **2005**, *4* (5), 366–377.

(2) Kang, B.; Ceder, G. *Nature* **2009**, *458* (7235), 190–193.

(3) Liu, X. H.; Zhang, L. Q.; Zhong, L.; Liu, Y.; Zheng, H.; Wang, J. W.; Cho, J.-H.; Dayeh, S. A.; Picraux, S. T.; Sullivan, J. P.; Mao, S. X.; Ye, Z. Z.; Huang, J. Y. *Nano Lett.* **2011**, *11* (6), 2251–2258.

(4) Obrovac, M. N.; Christensen, L. *Electrochem. Solid-State Lett.* **2004**, *7* (5), A93–A96.
(5) Obrovac, M. N.; Krause, L. J. *J. Electrochem. Soc.* **2007**, *154* (2), A103–A108.
(6) Liu, X. H.; Zheng, H.; Zhong, L.; Huang, S.; Karki, K.; Zhang, L. Q.; Liu, Y.; Kushima, A.; Liang, W. T.; Wang, J. W.; Cho, J.-H.; Epstein, E.; Picraux, S. T.; Zhu, T.; Li, J.; Sullivan, J. P.; Cumings, J.; Wang, C.; Mao, S. X.; Zhang, S.; Huang, J. Y. Anisotropic volume expansion and ultrafast lithiation of Si nanowires revealed by in-situ transmission electron microscopy. In *E-Beam Microcharacterization Centers & Nanoscale Science Research Centers 2011 Contractors' Meeting, Annapolis, Maryland, May 31 to June 2, 2011*;U.S. Department of Energy, Office of Basic Energy Sciences and Scientific User Facilities Division: Annapolis, MD, May 31 to June 2, 2011; p 147.
(7) Beaulieu, L. Y.; Eberman, K. W.; Turner, R. L.; Krause, L. J.; Dahn, J. R. *Electrochem. Solid State Lett.* **2001**, *4* (9), A137–A140.
(8) Chan, C. K.; Peng, H. L.; Liu, G.; McIlwrath, K.; Zhang, X. F.; Huggins, R. A.; Cui, Y. *Nat. Nanotechnol.* **2008**, *3* (1), 31–35.
(9) Kasavajjula, U.; Wang, C. S.; Appleby, A. J. *J. Power Sources* **2007**, *163* (2), 1003–1039.
(10) Cui, L. F.; Ruffo, R.; Chan, C. K.; Peng, H. L.; Cui, Y. *Nano Lett.* **2009**, *9* (1), 491–495.
(11) Park, M. H.; Kim, M. G.; Joo, J.; Kim, K.; Kim, J.; Ahn, S.; Cui, Y.; Cho, J. *Nano Lett.* **2009**, *9* (11), 3844–3847.
(12) Zhang, Q.; Zhang, W.; Wan, W.; Cui, Y.; Wang, E. *Nano Lett.* **2010**, *10* (9), 3243–3249.
(13) Teki, R.; Datta, M.; Krishnan, R.; Parker, T.; Lu, T.; Kumta, P.; Koratkar, N. *Small* **2009**, 2236–2242.
(14) Limthongkul, P.; Jang, Y.; Dudney, N.; Chiang, Y. *J. Power Sources* **2003**, 604–609.
(15) Limthongkul, P.; Jang, Y. I.; Dudney, N. J.; Chiang, Y. M. *Acta Mater.* **2003**, *51* (4), 1103–1113.
(16) Chevrier, V. L.; Zwanziger, J. W.; Dahn, J. R. *J. Alloys Compd.* **2010**, *496* (1−2), 25–36.
(17) Ng, S.; Wang, J.; Wexler, D.; Konstantinov, K.; Guo, Z.; Liu, H. *Angew. Chem., Int. Ed.* **2006**, 6896–6899.
(18) Key, B.; Bhattacharyya, R.; Morcrette, M.; Seznec, V.; Tarascon, J. M.; Grey, C. P. *J. Am. Chem. Soc.* **2009**, *131* (26), 9239–9249.
(19) Beattie, S. D.; Larcher, D.; Morcrette, M.; Simon, B.; Tarascon, J. M. *J. Electrochem. Soc.* **2008**, *155* (2), A158–A163.
(20) Larcher, D.; Beattie, S.; Morcrette, M.; Edstroem, K.; Jumas, J.; Tarascon, J. *J. Mater. Chem.* **2007**, 3759–3772.
(21) Zhou, S.; Liu, X. H.; Wang, D. W. *Nano Lett.* **2010**, *10* (3), 860–863.
(22) Huggins, R. A.; Nix, W. D. *Ionics* **2000**, *6*, 57–63.
(23) Tarascon, J. M.; Armand, M. *Nature* **2001**, *414* (6861), 359–367.
(24) Li, H.; Huang, X. J.; Chen, L. Q.; Zhou, G. W.; Zhang, Z.; Yu, D. P.; Mo, Y. J.; Pei, N. *Solid State Ionics* **2000**, *135* (1−4), 181–191.
(25) Magasinski, A.; Dixon, P.; Hertzberg, B.; Kvit, A.; Ayala, J.; Yushin, G. *Nat. Mater.* **2010**, *9* (4), 353–358.
(26) Beaulieu, L. Y.; Hatchard, T. D.; Bonakdarpour, A.; Fleischauer, M. D.; Dahn, J. R. *J. Electrochem. Soc.* **2003**, *150* (11), A1457–A1464.
(27) Hatchard, T. D.; Dahn, J. R. *J. Electrochem. Soc.* **2004**, *151* (6), A838–A842.
(28) Li, J.; Dahn, J. R. *J. Electrochem. Soc.* **2007**, *154* (3), A156–A161.
(29) Saint, J.; Morcrette, M.; Larcher, D.; Laffont, L.; Beattie, S.; Peres, J. P.; Talaga, D.; Couzi, M.; Tarascon, J. M. *Adv. Funct. Mater.* **2007**, *17* (11), 1765–1774.
(30) Larcher, D.; Beattie, S.; Morcrette, M.; Edstroem, K.; Jumas, J. C.; Tarascon, J. M. *J. Mater. Chem.* **2007**, *17* (36), 3759–3772.
(31) Sethuraman, V. A.; Chon, M. J.; Shimshak, M.; Srinivasan, V.; Guduru, P. R. *J. Power Sources* **2010**, *195* (15), 5062–5066.
(32) Limthongkul, P.; Jang, Y. I.; Dudney, N. J.; Chiang, Y. M. *J. Power Sources* **2003**, *119*, 604–609.
(33) Huang, J. Y.; Zhong, L.; Wang, C. M.; Sullivan, J. P.; Xu, W.; Zhang, L. Q.; Mao, S. X.; Hudak, N. S.; Liu, X. H.; Subramanian, A.; Fan, H. Y.; Qi, L. A.; Kushima, A.; Li, J. *Science* **2010**, *330* (6010), 1515–1520.
(34) Yamamoto, K.; Iriyama, Y.; Asaka, T.; Hirayama, T.; Fujita, H.; Fisher, C. A. J.; Nonaka, K.; Sugita, Y.; Ogumi, Z. *Angew. Chem., Int. Ed.* **2010**, *49* (26), 4414–4417.
(35) Chiang, Y. M. *Science* **2010**, *330* (6010), 1485–1486.
(36) Liu, X. H.; Zhong, L.; Zhang, L. Q.; Kushima, A.; Mao, S. X.; Li, J.; Ye, Z. Z.; Sullivan, J. P.; Huang, J. Y. *Appl. Phys. Lett.* **2011**, *98* (18), 183107.
(37) Zhang, L. Q.; Liu, X. H.; Liu, Y.; Huang, S.; Zhu, T.; Gui, L.; Mao, S. X.; Ye, Z. Z.; Wang, C. M.; Sullivan, J. P.; Huang, J. Y. *ACS Nano* **2011**, *5*, 4800–4809.
(38) Zhong, L.; Liu, X. H.; Wang, G. F.; Mao, S. X.; Huang, J. Y. *Phys. Rev. Lett.* **2011**, *106* (24), 248302.
(39) Islam, M. M.; Bredow, T.; Minot, C. *J. Phys. Chem. B* **2006**, *110* (19), 9413–9420.
(40) Strange, J. H.; Rageb, S. M.; Chadwick, A. V.; Flack, K. W.; Harding, J. H. *J. Chem. Soc., Faraday Trans.* **1990**, *86* (8), 1239–1241.
(41) Goel, P.; Choudhury, N.; Chaplot, S. L. *Phys. Rev. B* **2004**, *70* (17), 174307.
(42) Nesper, R.; Vonschnering, H. G. *J. Solid State Chem.* **1987**, *70* (1), 48–57.
(43) Seidel, H.; Csepregi, L.; Heuberger, A.; Baumgartel, H. *J. Electrochem. Soc.* **1990**, *137* (11), 3612–3626.
(44) Wu, B. Q.; Kumar, A.; Pamarthy, S. *J. Appl. Phys.* **2010**, *108* (5), 051101.
(45) Madou, M. J. *Fundamentals of Microfabrication: The Science of Miniaturization*, 2nd ed.; CRC Press: Boca Raton, FL, 2002; p 752.
(46) Hsueh, C. H.; Evans, A. G. *J. Appl. Phys.* **1983**, *54* (11), 6672–6686.
(47) Mott, N. F.; Rigo, S.; Rochet, F.; Stoneham, A. M. *Philos. Mag. B* **1989**, *60* (2), 189–212.
(48) Haftbaradaran, H.; Song, J.; Curtin, W. A.; Gao, H. J. *J. Power Sources* **2011**, *196* (1), 361–370.
(49) Zhao, K.; Wang, W. L.; Gregoire, J.; Pharr, M.; Suo, Z.; Vlassak, J.; Kaxiras, E. *Nano Lett.* **2011**, doi:10.1021/nl201501s.
(50) Zhao, K. J.; Pharr, M.; Vlassak, J. J.; Suo, Z. G. *J. Appl. Phys.* **2011**, *109* (1), 016110.

Supporting Information

Anisotropic swelling and fracture of silicon nanowires during lithiation

Xiao Hua Liu,[1] He Zheng,[2] Li Zhong,[2] Shan Huang,[3] Khim Karki,[4] Li Qiang Zhang,[2,10] Yang Liu,[1] Akihiro Kushima,[5] Wen Tao Liang,[6] Jiang Wei Wang,[2] Jeong-Hyun Cho,[7] Eric Epstein,[4] Shadi A. Dayeh,[7] S. Tom Picraux,[7] Ting Zhu,[3*] Ju Li,[5,8*] John P. Sullivan,[1] John Cumings,[4] Chunsheng Wang,[9] Scott X. Mao,[2] Zhi Zhen Ye,[10] Sulin Zhang[6], Jian Yu Huang[1*]

[1]Center for Integrated Nanotechnologies, Sandia National Laboratories, Albuquerque, New Mexico 87185, USA

[2]Department of Mechanical Engineering and Materials Science, University of Pittsburgh, Pittsburgh, Pennsylvania 15261, USA

[3]Woodruff School of Mechanical Engineering, Georgia Institute of Technology, Atlanta, Georgia 30332, USA

[4]Department of Materials Science and Engineering, University of Maryland, College Park, MD, 20742, USA

[5]Department of Materials Science and Engineering, University of Pennsylvania, Philadelphia, Pennsylvania 19104, USA

[6]Department of Engineering Science and Mechanics, Pennsylvania State University, University Park, Pennsylvania 16802, USA

[7]Center for Integrated Nanotechnologies, Los Alamos National Laboratory, Los Alamos, New Mexico 87545, USA

[8]State Key Laboratory for Mechanical Behavior of Materials and Frontier Institute of Science and Technology, Xi'an Jiaotong University, Xi'an, 710049, People's Republic of China

[9]Department of Chemical and Biomolecular Engineering, University of Maryland, College Park, MD, 20742, USA

[10]State Key Laboratory of Silicon Materials, Department of Materials Science and Engineering, Zhejiang University, Hangzhou, 310027, People's Republic of China

[*]Correspondence: jhuang@sandia.gov, ting.zhu@me.gatech.edu, liju@seas.upenn.edu

I. Experimental details

Preparation of Si nanowires. The Si nanowires were grown via a chemical vapor deposition (CVD) vapor-liquid-solid (VLS) growth method. The *n*-type Si nanowires were grown by passing 250 standard cubic centimeters (sccm) of silane (SiH_4, 50% diluted with argon) and 100 sccm of phosphine (PH_3, 100 ppm) at a pressure of 3 Torr across a Si substrate containing Au catalyst particles. The deposition temperature and time was 510 ºC and 30 minutes. The P/Si ratio was 1.0×10^{-4}.

Construction of the all-solid Si/Li_2O/Li electrochemical device. A small piece of Si wafer containing Si nanowires emerging from the surface was cleaved off from a large Si wafer growth substrate and glued to an aluminum rod with conductive epoxy (Fig. 1a). This ensured that there was good electrical contact between the nanowires and the Si substrate, which served as the primary current collector on the Si nanowire side. Lithium metal was scratched with a tungsten wire inside a glove box filled with helium (O_2 and H_2O content < 1 ppm). Both Si and Li electrodes were mounted onto a Nanofactory® TEM-scanning tunneling microscope (STM) holder inside a glove box. Then the holder was sealed in a home-built air-tight bag filled with dry helium and transferred to the TEM. The total time of exposure to the air was less than 2 s, which limited the extent of Li_2O formation on the surface of the Li metal. The liquid cell was constructed by replacing the Li metal with a bulk $LiCoO_2$ counter-electrode covered by one drop of the ionic liquid electrolyte (ILE, 10% LiTFSI dissolved in P_{14}TFSI; LiTFSI denoting lithium bis (trifluoromethylsulfonyl) imide and P_{14}TFSI denoting 1-butyl-1-methylpyrrolidinium bis (trifluoromethylsulfonyl) imide).[1]

II. Supporting Figures

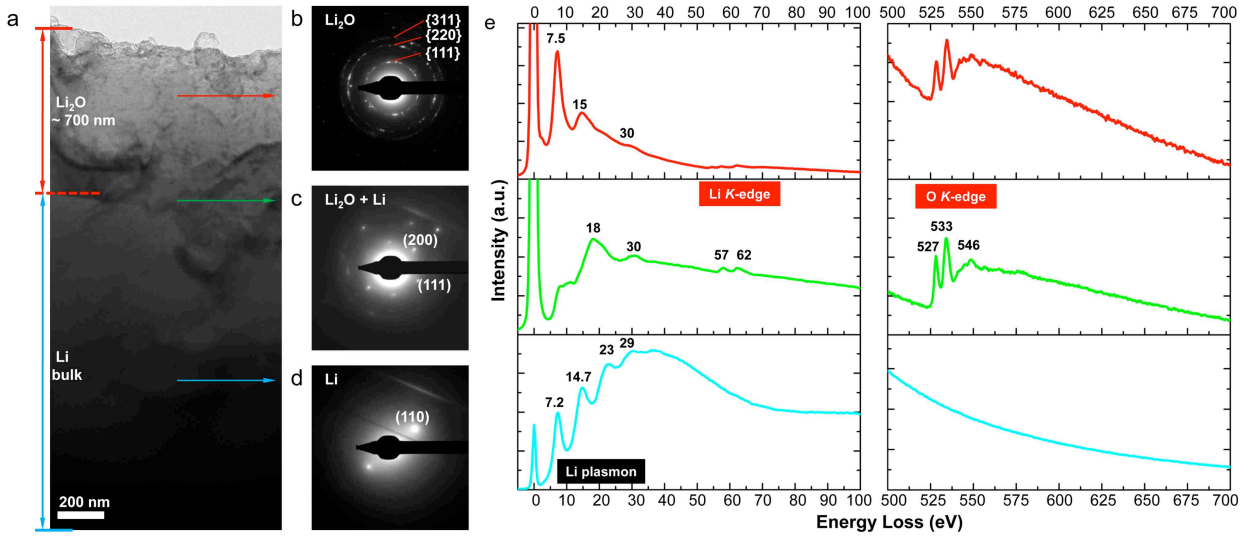

Figure S1. Characterization of the Li_2O solid electrolyte and Li electrode. (a) A typical view of the solid Li_2O/Li electrolyte/electrode. (b-d) Electron diffraction patterns (EDPs) from the Li_2O surface layer to the inner Li bulk showing the about 700-nm thick Li_2O on the Li metal. (e) Comparison of EELS spectra from the surface Li_2O layer to the inner Li region. In the low-loss region, multiple plasmon peaks were observed at 7.2, 14.4, 21.6, and 28.8 eV from the thick Li. The observed primary plasmon energy loss peak, E_p = 7.2 eV, agreed with the reported values for pure Li, which are in the range of 7.08 ~ 7.5 eV.[2] For the Li_2O thin layer, the low-loss peaks were different from those of Li metal, and the peak at 30.0 eV was relatively strong for thicker Li_2O (middle). Li *K*-edge peaks at 57.3 and 62.1 eV were much more obvious for Li_2O. The strong oxygen *K*-edge peaks with an onset around 520 eV were only visible in the Li_2O region.

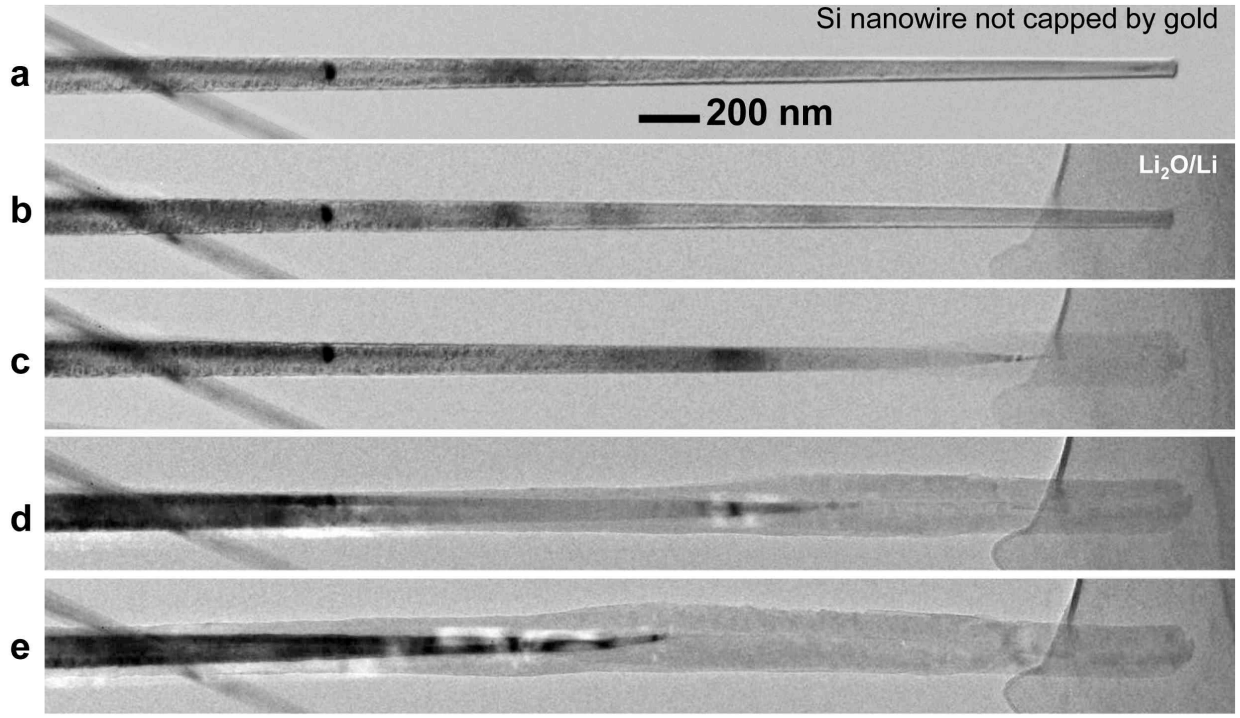

Figure S2. Similar lithiation behavior of a Si nanowire without a gold cap and directly touching Li_2O/Li. This indicates that the existence of a gold catalyst does not alter the lithiation behavior of the Si nanowire, which is intrinsic to the Li-Si alloying process.

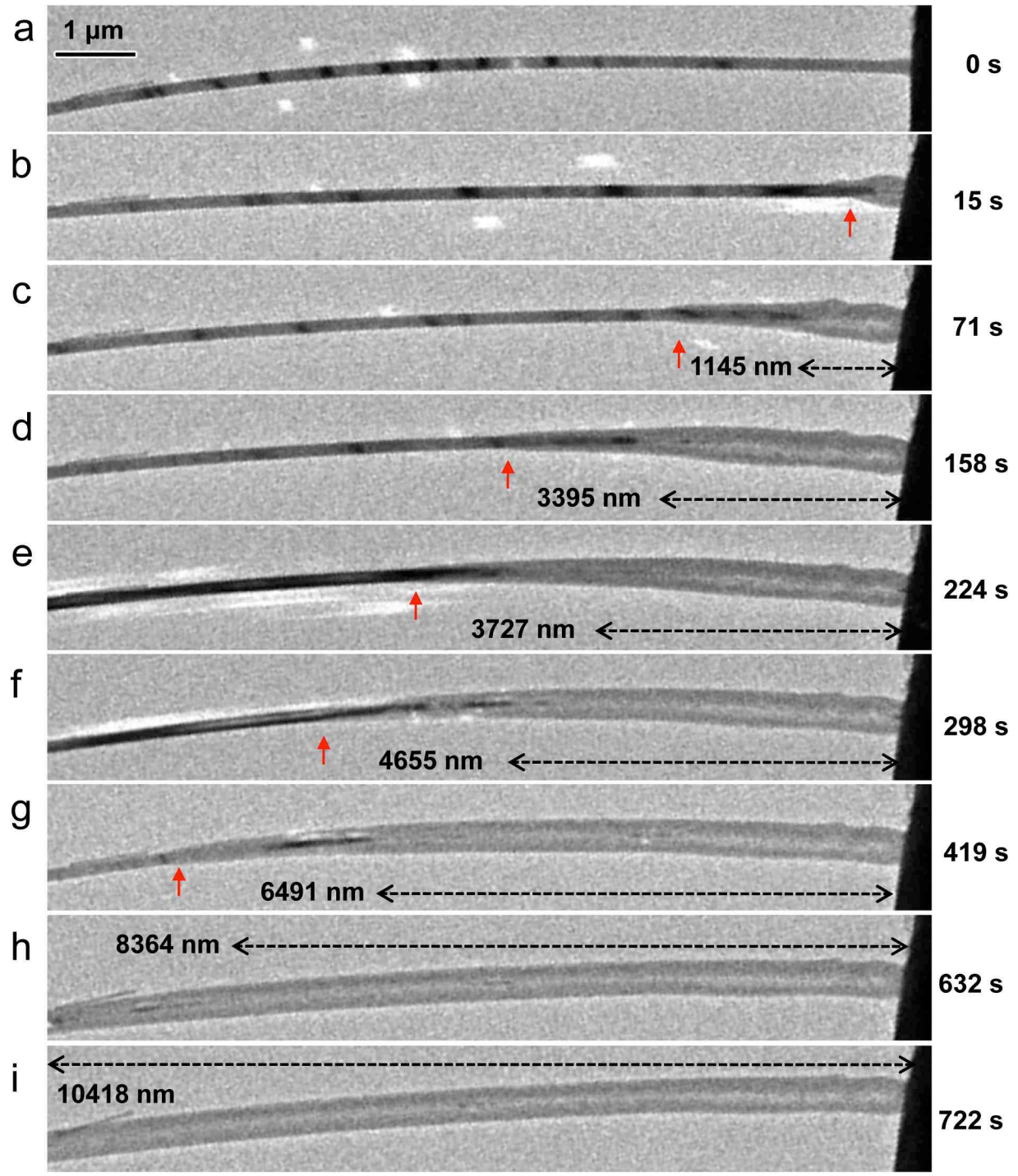

Figure S3. Crack formation during lithiation of another Si nanowire. As the reaction front (pointed out by red arrows) propagated, a crack extended following the tail of the conical residual *c*-Si core in the center of the nanowire.

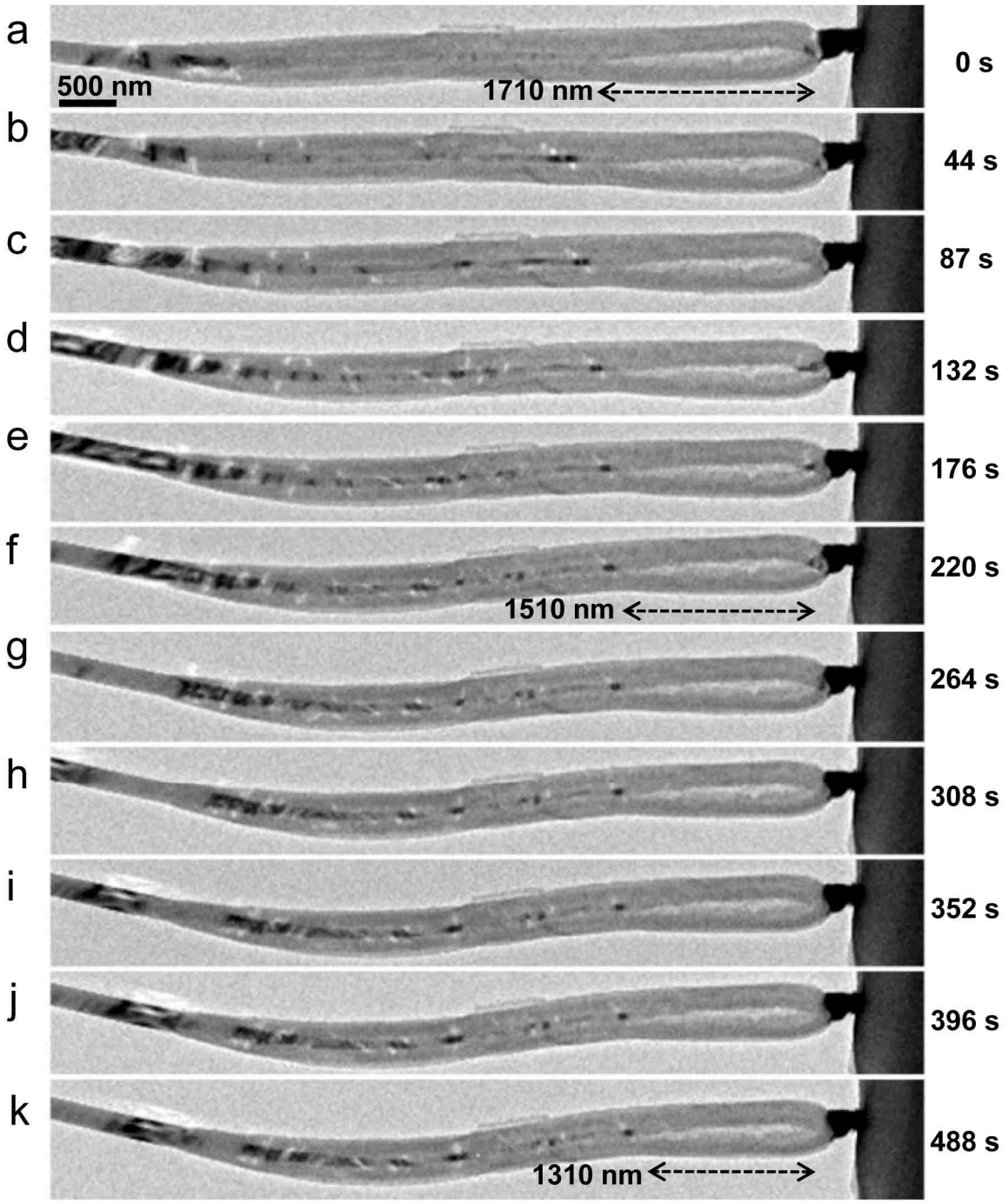

Figure S4. Crack and nanowire morphology evolution during delithiation of the same wire shown in Fig. 2. The nanowire was bent due to shrinkage after Li was extracted from the shell. The length of the crack also decreased from 1710 nm to 1310 nm in 8 minutes.

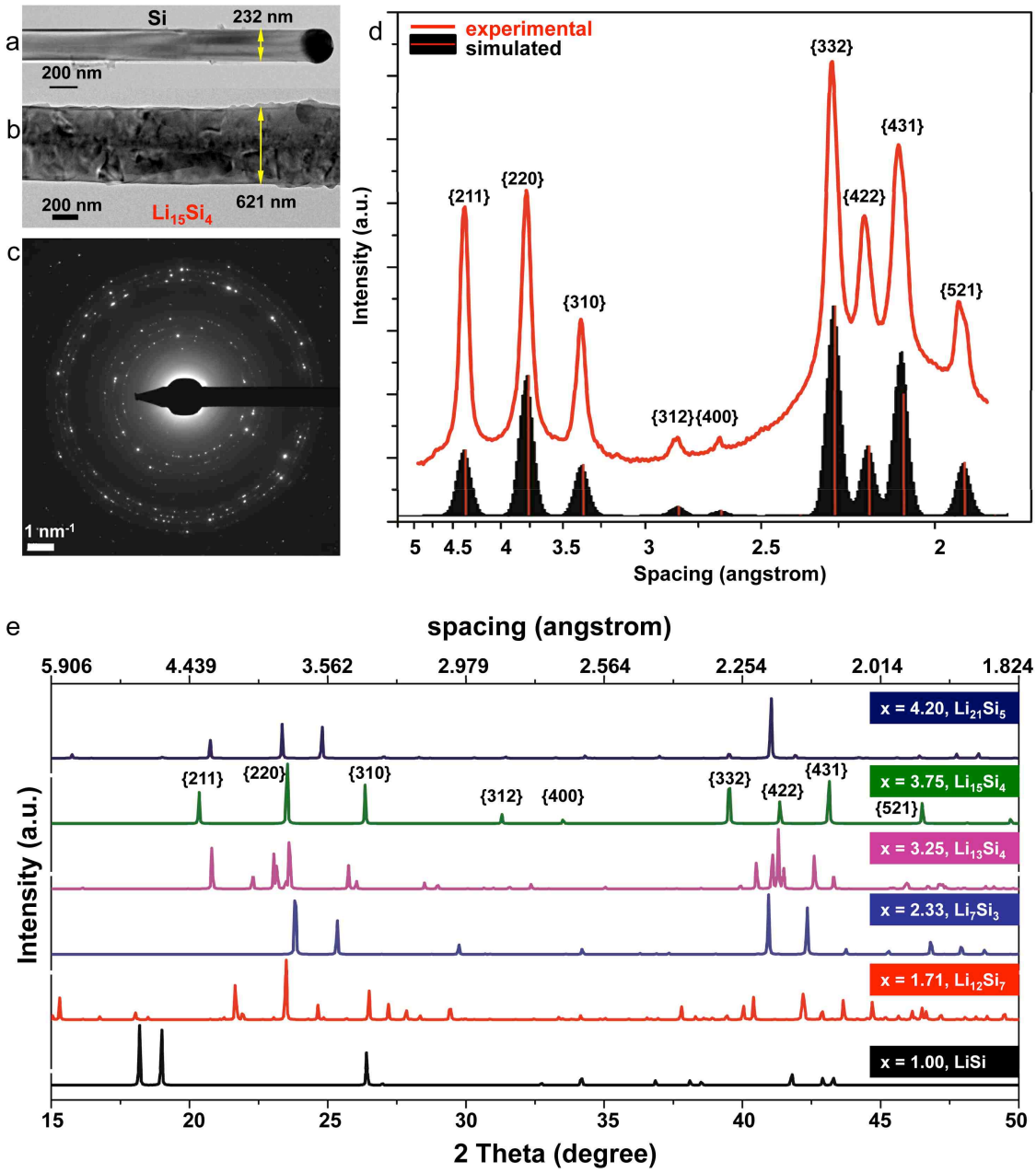

Figure S5. Identification of the $Li_{15}Si_4$ phase as the fully lithiated phase. (a) Pristine Si nanowire. (b-c) Lithiated Si nanowire (b) and its EDP (c). (d) Comparison of the intensity profiles of the experimental EDP and simulated EDP of the $Li_{15}Si_4$ phase, with excellent agreement for the nine observed strong diffraction rings. (e) Simulated X-ray diffraction patterns of the known Li-Si alloy phases with distinctive features. Note that for clarity, the pattern from the $Li_{22}Si_5$ phase is not presented here, because it resembles the pattern of the $Li_{21}Si_5$ phase due to almost identical atomic arrangement. The indices are only labeled for the observed $Li_{15}Si_4$ phase.

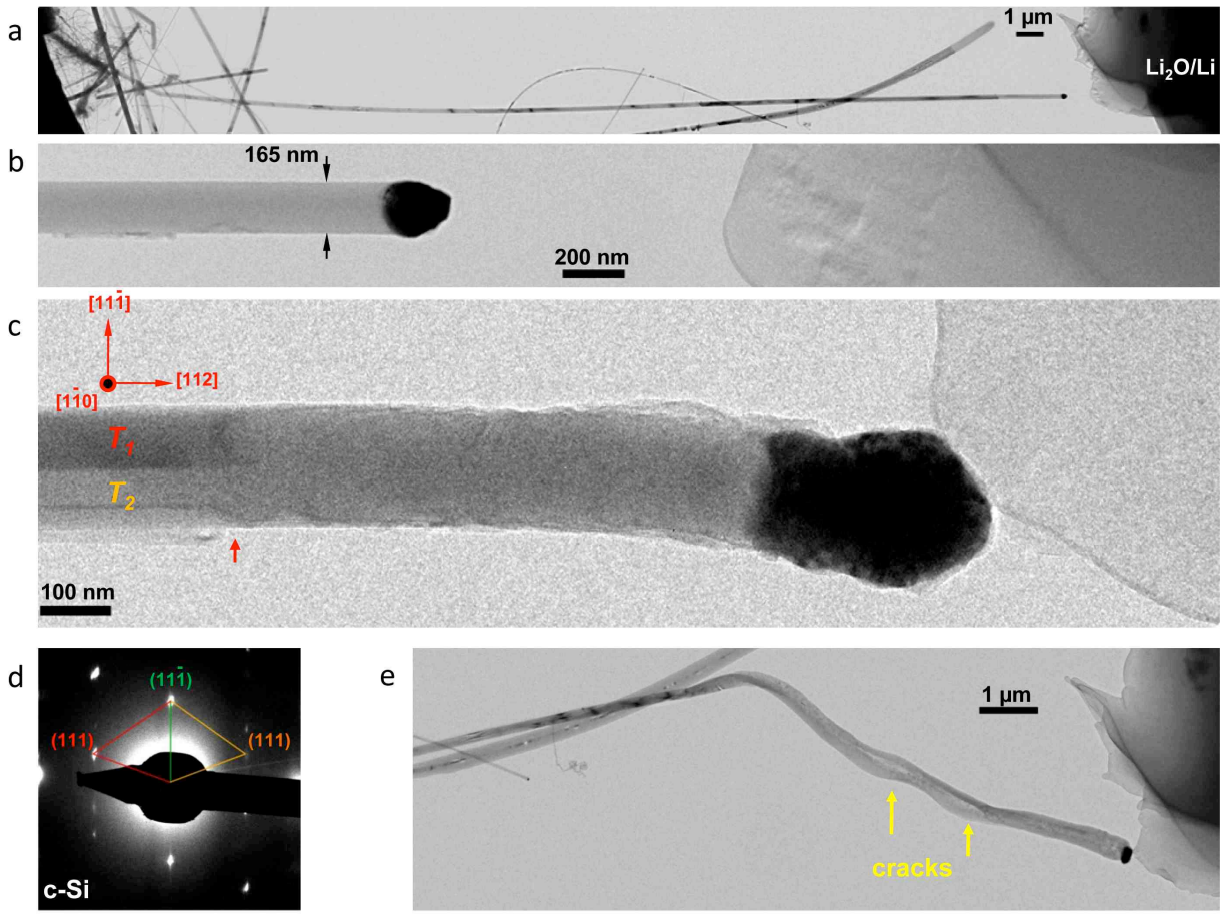

Figure S6. Lithiation of another [112]-oriented Si nanowire showing little expansion when viewed along the $[1\bar{1}0]$ direction. (a-b) Pristine Si nanowire. (c) Morphology of the nanowire in an intermediate state of lithiation. The red arrow marks the reaction front. A twin boundary was visible on the left side in the unreacted portion of the Si nanowire. Different image contrast on the left and right side of the reaction front is noticeable. The Au cap was elongated due to lithiation. Little expansion was seen along the $[11\bar{1}]$ direction. (d) Electron diffraction pattern from the pristine Si nanowire revealing the twin structure, consistent with the orientation relation shown in (c). (e) Tilted image showing cracks and a belt morphology of the lithiated nanowire.

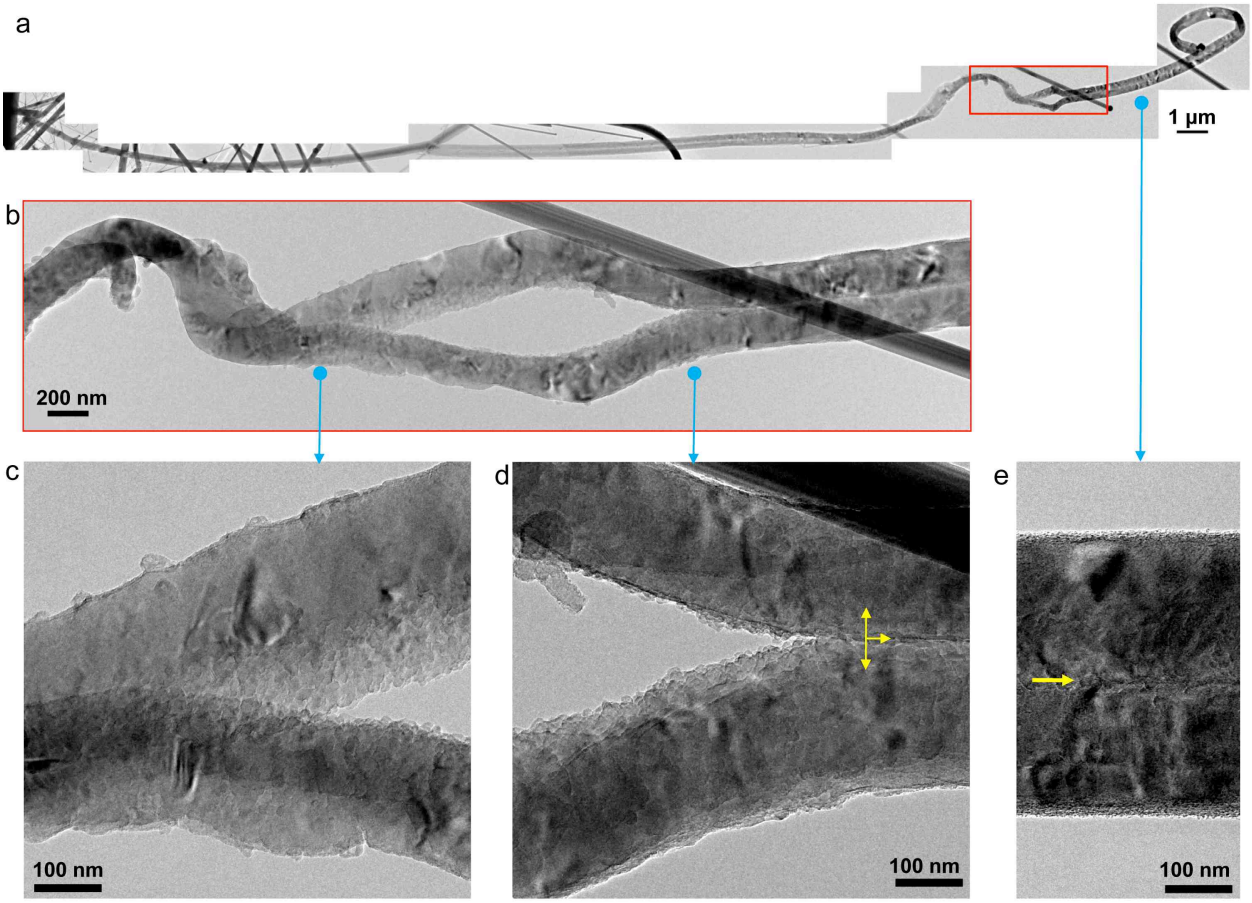

Figure S7. Self-splitting of a nanowire from the central crack during lithiation. (a) Low magnification TEM image of the lithiated nanowire. For this lithiation treatment, the potential for lithiation was –4 V with respect to Li metal. (b) Enlarged image showing the splitting/fracture of the nanowire. (c-d) Close-up views of the crease where the nanowire was split into two sub-wires. The yellow arrows mark the splitting directions and the central crack. (e) Non-split part with the central crack (marked by the yellow arrow).

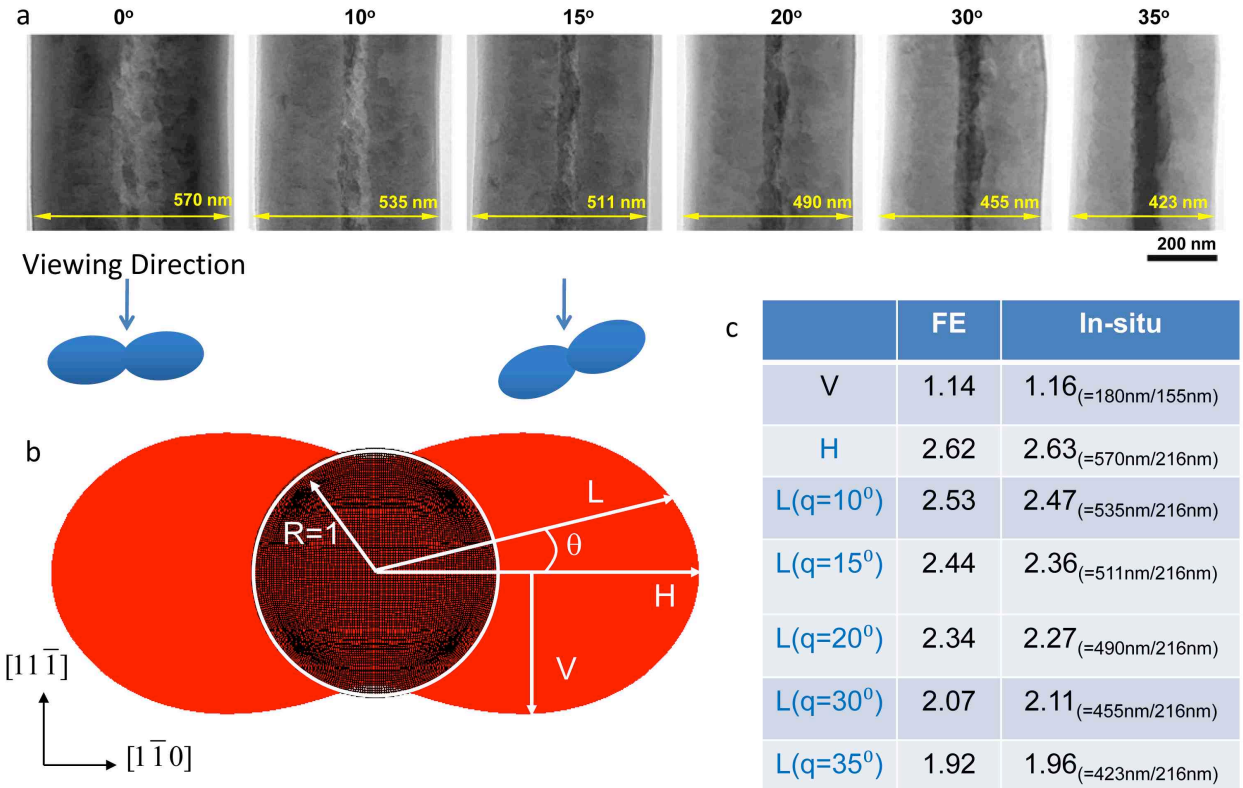

c

	FE	In-situ
V	1.14	$1.16_{(=180nm/155nm)}$
H	2.62	$2.63_{(=570nm/216nm)}$
L(q=10^0)	2.53	$2.47_{(=535nm/216nm)}$
L(q=15^0)	2.44	$2.36_{(=511nm/216nm)}$
L(q=20^0)	2.34	$2.27_{(=490nm/216nm)}$
L(q=30^0)	2.07	$2.11_{(=455nm/216nm)}$
L(q=35^0)	1.92	$1.96_{(=423nm/216nm)}$

Figure S8. Comparison of the cross-sectional geometry between experiment and simulation. (a) TEM images of the wire viewed from the side at different tilt angles. Because of the dumbbell-shaped cross section, the width of the wire, measured from the 2D projected view, changes with the viewing angle. Notice that the width of the Si core (in dark grey) increases with the viewing angle θ; this indicates that the cross section of the Si core has an elliptical shape. (b) The simulated cross section of a fully lithiated nanowire, showing the anisotropic volume expansion and final dumbbell cross section after full lithiation. The initial cross section of a pristine Si nanowire is represented by the circle enclosing the finite element (FE) mesh and it is superposed to highlight the morphological changes. (c) Quantitative comparison of the cross-sectional geometry between finite element method simulation and in-situ TEM measurement, the table lists the ratios of the characteristic lengths L, V and H of the lithiated wire, defined in (b), to the initial diameter (216nm) of the pristine wire. The overall error is less than 4%.

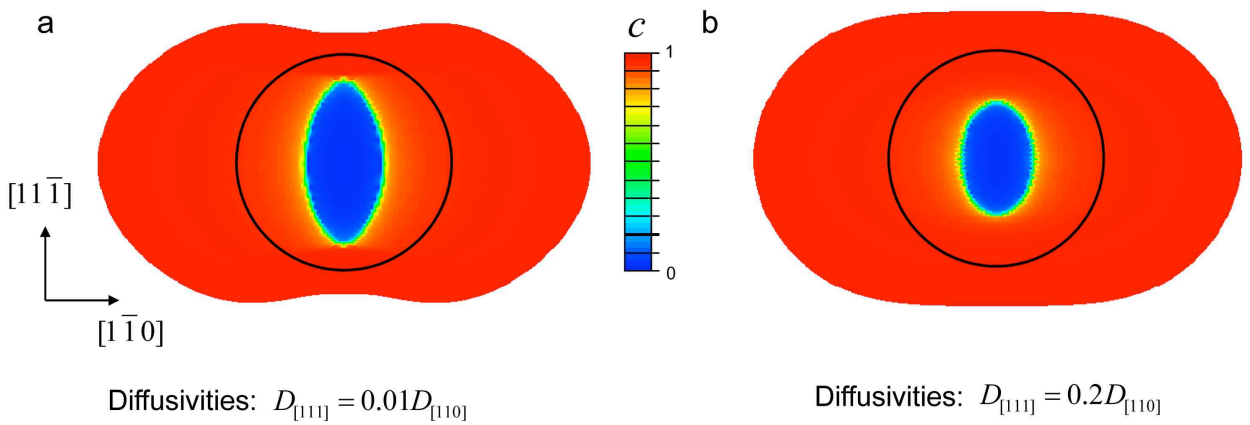

Figure S9. Sensitivity study of the Li diffusivity anisotropy on the necking instability. The Li distribution is compared when the diffusivity in the $[11\bar{1}]$ direction is (a) 0.01 times versus (b) 0.2 times that in the $[1\bar{1}0]$ direction. In case (a), the Si core is significantly elongated in the $[11\bar{1}]$ direction. In case (b), the elongation is significantly reduced, and the necking instability is consequently suppressed. Black circles indicate the initial cross section of the pristine Si nanowire.

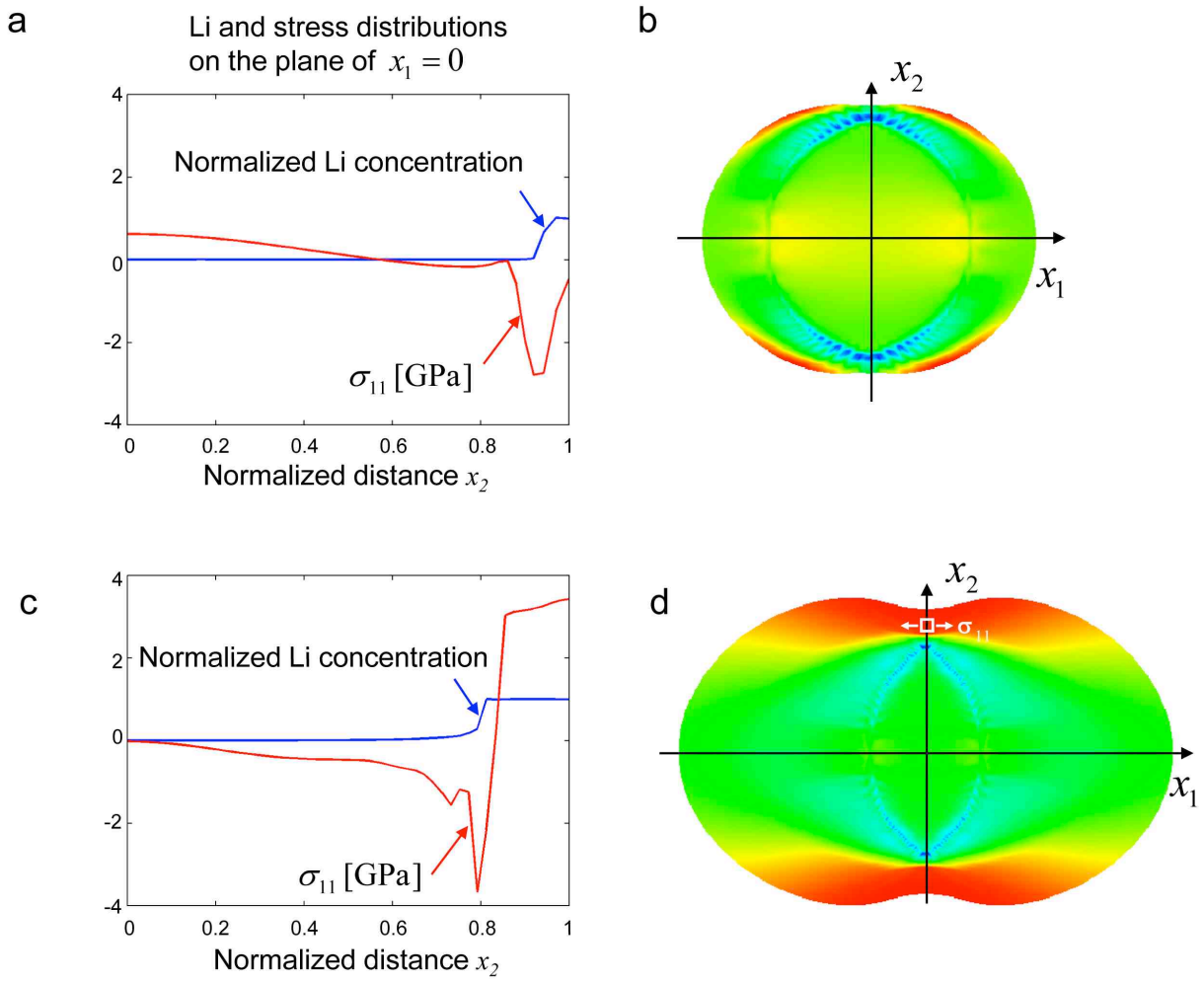

Figure S10. Distributions of Li and normal stress σ_{11} on the $x_2 - x_3$ plane at different deformation stages. (a-b) In the pre-necking stage, the lithiation reaction front (*i.e.* the region where the normalized Li concentration jumps from zero to one) is close to the surface, and σ_{11} is *compressive near the surface* and *tensile in the center*. (c-d) In the post-necking stage, the reaction front moves towards the center; σ_{11} becomes *tensile near the surface* and *compressive throughout the center*.

III. Supporting Movies

nl201684d_si_002.mpg, nl201684d_si_003.mpg, nl201684d_si_004.mpg
***In-situ* TEM movies showing the dumbbell cross-section of the lithiated Si nanowires.** The videos were recorded at 3 frames/s and played at 10× (**nl201684d_si_002.mpg**) and 50× (**nl201684d_si_003.mpg**, **nl201684d_si_004.mpg**) speed.

nl201684d_si_005.mpg, nl201684d_si_006.mpg, nl201684d_si_007.mpg
***In-situ* TEM movies showing the lithiation of Si nanowires**. Note the volume expansion after the reaction front passed by and crack nucleation and propagation along the tail of the *c*-Si core. The videos were recorded at 3 frames/s and played at 50× (**nl201684d_si_005.mpg**, **nl201684d_si_006.mpg**) and 100× (**nl201684d_si_007.mpg**) speed.

nl201684d_si_008.mpg
3D simulation of the Li distribution and anisotropic swelling in a progressively-lithiated Si nanowire.

nl201684d_si_009.mpg
Same as Movie nl201684d_si_008.mpg, except that the wire is cut to expose the Li distribution in the (111) cross section, showing the development of the tapered core-shell structure along the longitudinal direction of the nanowire.

nl201684d_si_010.mpg
2D simulation of the cross-sectional Li distribution, showing the development of the core-shell structure and dumbbell-shaped cross section due to the onset and growth of a necking instability.

nl201684d_si_011.mpg
Same as Movie nl201684d_si_010.mpg, except that the distribution of the von Mises equivalent stress is plotted, showing the development of extensive plastic flow due to progressive lithiation (red indicates attainment of the plastic yield stress).

IV. Identification of $Li_{15}Si_4$ as the final lithiated phase

The calculated structure factors (F) and extinction distances (ξ) of the observed diffracted beams are listed in Table S1. All the *hkl* diffraction rings are in excellent agreement with the experimental EDPs from the lithiated Si nanowires (Fig. S5). Kinetical approximation was valid because the smallest ξ for {332} plane family is about 334.3 nm (highlighted in red in Table S1), larger than the thickness of the $Li_{15}Si_4$ nanowire, ~ 250 nm (Figs. S4a-S4b, note that the e-beam incident and view directions were close to <111> because Fig. S4b showed large diameter expansion).

The XRD patterns in Fig. S4e were generated with Materials Studio® using atomic coordinates of the six known Li_xSi phases listed in Dahn *et al.*'s publication.[3] The widely assumed phase for fully lithiated Si, *i.e.* $Li_{22}Si_5$, is very similar to the $Li_{21}Si_5$ in atomic arrangement.[4] As a result, the XRD patterns are very similar thus not piled in Fig. S4e.

Table S1. Structure factors and extinction distances of the observed 9 diffraction rings.

hkl	Spacing/Å	Structure Factor (F)	Amptitude of F, $\|F\|^2$	Multiplication of *hkl*	Extinction Distance, ξ/nm
211	4.350	-0.483-0.784*i*	0.921	24	829.7
220	3.767	2.044+0.080*i*	2.046	12	373.5
310	3.369	0.038-0.912*i*	0.913	24	837.2
312	2.848	0.282-0.085*i*	0.295	48	2593.5
400	2.664	0.606+0.029*i*	0.607	6	1258.3
332	2.272	-1.463-1.756*i*	2.285	24	334.3
422	2.175	1.079+0.795*i*	1.340	24	570.2
431	2.090	-0.608-0.480*i*	0.774	48	986.7
521	1.945	-0.251-0.832*i*	0.869	48	879.4

V. Description of modeling

We have performed both three-dimensional (3D) and two-dimensional (2D) simulations to explore the effects of lithiation on the morphology changes and fracture in Si nanowires. To simulate the development of the core-shell structure, we implemented a Li diffusion model with Li concentration-dependent diffusivities, facilitating the formation of a sharp interface that separates the Li-poor core (*i.e.*, the ratio of Li to Si $x \approx 0$) and Li-rich ($x \approx 3.75$) shell. Note that our simulations mainly serve to generate a sequence of core-shell structures for the mechanics analyses of deformation and fracture, rather than provide a precise description of the mechanisms of the dynamic lithiation process, which would be difficult due to lack of experimental measurements for model calibration.[5-7] To this end, we employed a simple non-linear function on diffusivity

$$D = D_0\left[1/(1-c) - 2\Omega c\right] \qquad (1)$$

where D_0 is the diffusivity constant, c is the normalized Li concentration defined as the ratio between actual Li concentration divided by the Li concentration at the fully lithiated state (x = 3.75). On the basis of the free energy function of a regulation solution model, $f = \Omega c(1-c) + \left[c\ln c + (1-c)\ln(1-c)\right]$, diffusivity D in Eq. (1) was derived according to a definition that can sharply increase diffusivities at high Li concentrations, $D = D_0 c d^2 f / dc^2$. In diffusion simulations, the normalized lithium concentrations behind the reaction front can quickly attain the high values (slightly below 1), while those ahead of the front remain nearly zero. This produces a sharp reaction front that is consistent with experimental observation, thereby providing a basis of further stress analysis. It should be noted that a small gradient of lithium concentration still exists behind the reaction front, so that Li can diffuse through the lithiated shell continuously to move forward the reaction front to the center of the wire. The non-linear relation of Eq. (1) is unbounded at $c = 1$; for numerical stability, the maximum of D is capped at $10^4 D_0$. In Eq. (1), the parameter Ω can be tuned to control the concentration profile near the reaction front, and we took Ω = 3 for achieving the numerical stability.

In order to account for the influence of crystalline Si core on the migration velocity of the core-shell interface, the apparent Li diffusivity was assumed to be crystal orientation dependent. Such anisotropy plays a critical role in the formation of the dumbbell-shaped cross section, as numerically shown next. Among the non-zero direct components of diffusivity, D_{ij}, our numerical experiments indicated that D_{11} in the $[1\bar{1}0]$ direction should be about 100 times D_{22} in the $[11\bar{1}]$ direction. It should be emphasized that the assignment of anisotropic diffusivities serves as an effective numerical approach to capture the orientation-dependent migration velocity of the lithiation reaction front. Specifically, the anisotropic diffusivity in a "single phase" we used in our "diffusion" simulation was adopted to describe the anisotropic movements of what are actually two-phase interfaces. In reality, the two phases are α = Si-Li alloy in diamond cubic crystal structure (with Li fraction no more than 20% from TEM observations), and β = $Li_{15}Si_4$ compound + Li_2O + amorphous Li_xSi (for simplicity we lump them all together and pretend they are one "product" phase), characterized by much higher Li concentrations. Microscopy evidences indicate the α–β interface is both structurally and chemically very sharp, and moves by the atomic-ledge mechanism (to be published). Thus, the transport and chemical

reaction aspect of this problem can be naturally divided into three parts: (1) Li bulk diffusion in α, (2) Li bulk diffusion in β, and (3) motion of the αβ interface where dramatic structural and chemical changes occur in the swept area. The physical origin of the anisotropy lies mostly in (3), even though (1) and (2) may have anisotropies also. The diffusivity model taken in our "single phase" simulation is just to mimic the anisotropic motion in (3) – as can be seen in Fig. 5, we indeed achieved rather sharp and moving interfaces that match with our experiments – the main purpose of our "diffusion" model. However, we would like to emphasize that the main point of our simulation is to compute the **stress distribution** due to lithiation transformation strain, that furthermore drives **plastic flow** and **fracture**, i.e. the mechanics part of the problem, not the transport and chemistry part. The rigorous framework for the transport and chemistry part is delayed to a future paper.

To mimic the fast Li diffusion at the surface,[8] the Li surface diffusivity was taken as 300 times the bulk diffusivity of D_{11}, giving the tapered core-shell structure in 3D finite element simulations, consistent with experimental observation, as discussed later.

We adopted an elastic and perfectly plastic model to describe the lithiation-induced deformation. The increment of the total strain, $d\varepsilon_{ij}$, is taken to be the sum of three contributions,[9]

$$d\varepsilon_{ij} = d\varepsilon_{ij}^{c} + d\varepsilon_{ij}^{e} + d\varepsilon_{ij}^{p} \qquad (2)$$

In Eq. (2), the increment of the lithiation-induced chemical strain, $d\varepsilon_{ij}^{c}$, is proportional to the increment of the normalized Li concentration, $d\varepsilon_{ij}^{c} = \beta_{ij} dc$. Here β_{ij} represents the expansion coefficient with non-zero direct components, and they are controlled by the atomic processes near the lithiation reaction front and are expected to be anisotropic for lithiation of *c*-Si. Since a mechanistically-based assignment of β_{ij} is beyond the scope of this work, we performed numerical experiments to determine β_{ij} by adjusting β_{ij} to give a close fit of the measured geometry of fully lithiated Si nanowires. By this procedure, we obtained $\beta_{11} = 150\%$ in <110>, $\beta_{22} = 40\%$ in <111>, and $\beta_{33} = 0$ in <112> directions.

In Eq. (2), the increment of the elastic strain, $d\varepsilon_{ij}^{e}$, obeys Hooke's law, $d\varepsilon_{ij}^{e} = \left[(1+\nu)d\sigma_{ij} - \nu d\sigma_{kk}\delta_{ij}\right]/E$, where E is Young's modulus and ν is Poisson's ratio, $\delta_{ij} = 1$ when $i = j$, $\delta_{ij} = 0$ otherwise, and the repeated index means summation. Our elasticity model accounts for the Li concentration-dependent E and ν; for pristine Si, E = 80 GPa, $\nu = 0.28$, and for fully lithiated Si, E = 30 GPa, $\nu = 0.24$; both E and ν linearly vary between the two limits as suggested by recent first-principles calculations.[10]

In Eq. (2), the increment of the plastic strain, $d\varepsilon_{ij}^{p}$, was assumed to obey the classic J_2-flow rule; namely plastic yielding occurs when the von Mises equivalent stress, $\sigma_{eq} = \sqrt{3 s_{ij} s_{ij}/2}$, equals the yield stress σ_Y. Here $s_{ij} = \sigma_{ij} - \sigma_{kk}\delta_{ij}/3$ is the deviatoric stress; $d\varepsilon_{ij}^{p}$ is proportional to s_{ij} and can be determined by solving the boundary value problem.

We numerically implemented the above diffusion and elastic-plastic model by using the finite element package ABAQUS 6.10.[11] The 3D simulation can well capture the overall wire deformation and development of the tapering core-shell structure, while the 2D cross-sectional simulation (with fine meshes) enables the quantification of geometry of a fully lithiated nanowire, which is consistent with experimental measurements. The Li and stress-strain fields were incrementally updated using an implicit coupled temperature-displacement procedure in ABAQUS/Standard. Specifically, the lithiation-induced strain was simulated by a thermal strain approach. That is, the normalized concentration was surrogated by temperature and the expansion coefficient β_{ij} was equivalently treated as the thermal expansion coefficient. The user material subroutine for heat transfer (UMATHT) was programmed to interface with ABAQUS for updating diffusivities based on the current Li concentration (*i.e.*, temperature). The Li distribution was then updated and so was the increment of the elastic-plastic deformation. In order to numerically stabilize the large distortions at both the reaction front and growing neck, a small rate sensitivity was used by assigning the exponent of 500 for the over-stress power law model of rate-dependent viscoplasticity.[11]

In 2D cross-sectional simulations, the plane-strain condition was assumed on the basis of the negligible axial deformation observed in experiments. We used the 4-node plane strain element with thermally coupled quadrilateral, bilinear displacement and temperature (CPE4T). The in-plane boundary conditions were taken as a constant Li concentration ($c = 1$) and zero tractions at the outer boundary. Utilizing the symmetry condition, one quarter of the wire was modeled to reduce the computation cost. For 3D simulations, the Li surface flux was prescribed at one end of the wire and a skin layer was additionally attached to the wire surface. As mentioned earlier, to mimic the fast Li diffusion at the surface, the Li diffusivity in this skin layer was taken as 300 times that in the bulk. The simulation of development of the core-shell structure (Movie S8) agrees with *in situ* TEM observations. In addition, the 3D simulation of distributions of the Li concentration and stresses are consistent with the results from 2D cross-sectional simulations. Such a close correlation can be understood by noting that our non-linear diffusivity model (Eq. 1) essentially forces the normalized Li concentrations to be close to either zero (pristine Si) or one (fully lithiated Si). As a consequence, the in-plane diffusion in 3D simulations occurs mostly under the condition of a fully-lithiated surface, which is the boundary condition in 2D simulations. Both our 2D and 3D simulations well captured the main features of the morphology changes in experiments.

We have performed numerical experiments to evaluate the sensitivity of our simulations to assigned Li diffusivities. Of particular note is the influence of the anisotropy of apparent Li diffusivities, which characterizes the orientation-dependent migration velocity of the lithiation reaction front, as discussed earlier. Figure S9 shows that an increase of such anisotropy can promote the elongation of the shrinking Si core in the $[11\bar{1}]$ direction, which is fundamentally needed to facilitate the necking instability. Specifically, in reference to the coordinate system in Fig. 5a of the text, let us focus on the lithiated shell near the apex of the cross section. As lithiation proceeds, if the thickness of such a shell, measured in the x_2 direction of $[11\bar{1}]$, can increase significantly with x_1, it will generate a large variation of the outward surface displacement, which increases with x_1. As a result, the top surface will gradually become flat and even slightly indented. The ensuing stress concentration at the indent facilitates the onset of

necking instability. Further post-necking deformation can lead to the formation of the observed dumbbell-shaped cross section.

The physical origin of the necking instability can be revealed by analyzing the elastic-plastic deformations of the surface layer near the apex of the cross section. Upon lithiation, a compressive hoop stress first develops in this layer, due to the circumferential constraint on volume expansion (Figs. S10a, S10b). This is followed by the compressive plastic yielding with a further increase of the local Li concentration. The layer becomes fully lithiated after the passing of the reaction front. As lithiation proceeds, the volume expansion at the lithiation front displaces the materials behind it in the outward radial direction and simultaneously stretches them in circumferential directions. As a result, the surface layer sequentially undergoes *compressive elastic unloading*, *tensile elastic loading* and *tensile plastic yielding* (Figs. 5e-5f and Figs. S10c, S10d). This is reminiscent of the deformation sequence at the crack tip under cyclic mechanical load.[12] It should be emphasized that the tensile plastic flow is only a necessary condition of a necking instability. Our simulations (Movies S7-S10) clearly show the non-uniform surface displacement near the apex of the cross section during the pre-necking deformation, mainly caused by the lithiation strain in the $[11\bar{1}]$ direction and promoted by the $[11\bar{1}]$-elongated Si core (Figs. S9a, 5d). Consequently, the surface near the apex gradually becomes flat and slightly indented. Driven by the progressive lithiation of the Si core, further expansion of the lithiated shell causes the onset of a necking instability around the surface indent, followed by neck growth and formation of the dumbbell-shaped cross section, consistent with experimental observation.

References:

1. Huang, J. Y.; Zhong, L.; Wang, C. M.; Sullivan, J. P.; Xu, W.; Zhang, L. Q.; Mao, S. X.; Hudak, N. S.; Liu, X. H.; Subramanian, A.; Fan, H. Y.; Qi, L. A.; Kushima, A.; Li, J. *Science* **2010,** 330 (6010), 1515-1520.
2. Liu, D. R.; Williams, D. B. *Philosophical Magazine B-Physics of Condensed Matter Statistical Mechanics Electronic Optical and Magnetic Properties* **1986,** 53 (6), L123-L128.
3. Chevrier, V. L.; Zwanziger, J. W.; Dahn, J. R. *Journal of Alloys and Compounds* **2010,** 496 (1-2), 25-36.
4. Nesper, R.; Vonschnering, H. G. *Journal of Solid State Chemistry* **1987,** 70 (1), 48-57.
5. Chiang, Y. M.; Tang, M.; Huang, H. Y.; Meethong, N.; Kao, Y. H.; Carter, W. C. *Chemistry of Materials* **2009,** 21 (8), 1557-1571.
6. Tang, M.; Carter, W. C.; Chiang, Y. M. *Annual Review of Materials Research, Vol 40* **2010,** 40, 501-529.
7. Bazant, M. Z.; Burch, D. *Nano Letters* **2009,** 9 (11), 3795-3800.
8. Zhang, Q.; Zhang, W.; Wan, W.; Cui, Y.; Wang, E. *Nano Letters* **2010,** 10 (9), 3243-3249.
9. Zhao, K. J.; Pharr, M.; Vlassak, J. J.; Suo, Z. G. *Journal of Applied Physics* **2011,** 109 (1), 016110.
10. Shenoy, V. B.; Johari, P.; Qi, Y. *Journal of Power Sources* **2010,** 195 (19), 6825-6830.
11. *SIMULIA, Providence, R.I.* **2010**.
12. Suresh, S., *Fatigue of Materials*. Cambridge University Press: Cambridge, UK, 1998.